The Fabrication and Physics of High-Efficiency CdTe Thin-Film Solar Cells

Final Technical Report for the Period
September 1, 2001 to August 31, 2004

Contract No. NDJ-1-30630-02

Alvin D. Compaan, principal investigator
Victor Karpov, co-principal investigator
Randy G. Bohn, co-investigator
Dean Giolando, co-investigator
Xunming Deng, co-investigator

NREL technical monitor: Ken Zweibel

Department of Physics and Astronomy
The University of Toledo
Toledo, OH 43606

Summary

There are three focus area in this subcontract: cell structure and fabrication, cell modelling, and characterization of materials and devices.

Our efforts on cell fabrication have primarily involved the use of magnetron sputtering for deposition. In addition, we have developed and used novel electrochemical treatments at the stage of finishing the devices deposited by other techniques: vapor transfer deposition (VTD) and close space sublimation (CSS), both made at First Solar, LLC. During the period of this award we have:

- achieved 12.6% efficiency in an all-sputtered cell on Tec-15 soda-lime glass,
- developed ZnO:Al as front contact and ZnTe:N as a back contact to substrate cells, achieved 14.0% efficiency on aluminosilicate glass with sputtered ZnO:Al/CdS/CdTe
- fabricated substrate CdS/CdTe solar cells using molybdenum foil, soda-lime glass, and SnO_2:F coated Tec 7 glass as substrates; developed a technology of depositing Molybdenum on glass for substrate cells, including identification of stresses responsible for film failure and their mitigation,
- developed a series of new high-resistivity transparent (HRT) buffer layers that improve the device efficiency and allows for the use of thin CdS,
- established a new buffer layer effect: 'doping without dopants', which enables one to achieve high open-circuit voltages and superior stability without the use of Cu,
- created a new class of electrolyte treatments that significantly change the device back contact, improve its uniformity, and can alone increase the cell efficiency from 3% to 11%,
- developed and experimentally verified a model of reach-through diode effect on back-contact properties,
- developed numerical modelling of current distribution in cells including nonuniformities in the main junction and back barrier; also, using comercial software Pspice, extended our modeling effort to large-area modules,

- built a quantitative theory establishing figure of merit for nonuniformity effects in thin-film cells and predicted a phase transition between the regimes of weakly nonuniform and strongly nonuniform cells,
- devised biased-dependent photoluminescence mapping that allows for identification of major device flaws,
- for the first time identified the phenomenon of PL fatigue in thin-film photovoltaics and related it to the light-soak induced degradation,
- studied properties of of ion-implanted defects in CdTe crystals,
- created a new admittance spectroscopy "tool kit" that enables one to separate out the defect related features in the admittance spectra of CdTe devices,
- by means of x-ray absorption fine structure (XAFS) studies, found that most Cu in CdTe cells is oxidized if chloride treatments have been used and that this Cu is probably concentrated at the grain boundaries,
- discovered the divergence in fluctuations of the main photovoltaic parameters under low light as a diagnostic tool for characterizing the device nonuniformity.

Table of Contents

Summary i

List of Figures v

List of Tables viii

1 Introduction 1

1.1 Background 1

1.2 Objectives of this subcontract 1

1.3 Technical approach 2

2 Cell Structure and Fabrication 3

2.1 CdS/CdTe Devices with a ZnO High Resistivity Buffer Layer 3

2.2 Sputtered ZnO:Al Layer as the Front Contact TCO 5

2.3 Work in progress 9

References (Section 2) 9

3 Cell Modeling 10

3.1 Overview 10

3.2 Reach-through band bending in semiconductor thin films 11

3.3 Modeling of non-uniformity losses in integrated large-area solar cell modules 17

3.4 Back contact and reach-through diode effects in thin-film photovoltaics . . 23

References (Section 3) 36

4 Characterization of materials and devices 40

4.1 Overview 40

4.2 Photoluminescence studies on ion-implanted CdTe crystals 40

4.3 Cu K-edge XAFS in CdTe before and after treatment with $CdCl_2$ 45

References (Section 4) 52

5 Publications 54

5.1 Refereed papers published or in press (9/1/01 - 8/31/04) 54

5.2 Poster or oral presentations published on CDROM and the NREL Web site 56

5.3 Contributed oral or poster presentations (no published manuscript) 56

5.4 Annual Subcontract Reports Summary published in U.S. Dept. of Energy Photovoltaic Energy Program Contract Summary, FY 2002, 2003 57

6 Project personnel 58

6.1 Research professors 58
6.2 Postdoctoral Associate 58
6.3 Graduate Students (with Principal Advisor) 58
6.4 Undergraduate students 59
6.5 Technical Assistants 59

List of Figures

2.1 External quantum efficiency of best cells prepared on SnO_2 and ZnO HR layers. 4

2.2 I-V and QE plots of CdS/CdTe solar cell on ZnO:Al and SnO_2 TCO. 6

2.3 Changes in V_{oc}, FF, J_{sc} and efficiency with light soak time. 7

3.4 Energy-band diagrams for a system of metal, semiconductor thin-film, bulk semiconductor (a) before contact, (b) after contact as predicted by the standard Schottky barrier formation scenario, (c) after contact accompanied by acceptor defect generation. 12

3.5 J-V curves (a) and Open circuit voltage (V_{oc}) and short-circuit current (J_{sc}) (b) for Cu doped and undoped CdS/CdTe structures with and without buffer layer. 15

3.6 QE characteristics of CdS/CdTe structures without (a) and with (b) buffer layer for different voltages before and after Cu diffusion. 15

3.7 C-V characteristics of CdS/CdTe structures without (a) and with (b) buffer layer before and after Cu diffusion. In the graph (a) the data are truncated to $V < 0.5$ V to avoid the conduction contribution indicated by the phase angle between the real and imaginary parts of the measured admittance. . . 16

3.8 Random diode array with lump parameters: row (scribe) resistance R_r, series resistance R_s, and shunt resistance R_{sh}. Fat lines represent electrodes (bus bars) used to measure the system current and voltage. 18

3.9 Sketch of integrated photovoltaic module on a monolithic (typically glass) substrate. Tilted fragments between cells represent interconnections through scribes. 19

3.10 Disorder in V_{oc}. a) Generated statistical V_{oc} distributions - continuous and bi-modal (note the log scale), with the same average value $< V_{oc} >$=755 mV, standard deviation SD=100, relative dispersion $\delta = 13\%$; b) Maps of 29 by 58 diodes illustrate topological realization for corresponding statistical distributions. Relative efficiency $\eta_{rel} = 0.92$ is the same in both cases. 20

3.11 Standard deviation (SD) changes almost by 2 orders of magnitude from the smallest to the largest module (note a log-log scale). The cases of fluctuating V_{oc} and J_{sc} are shown. Straight lines represent linear fits. 21

3.12 Size dependence of the module mismatch loss for the cases of randomly distributed V_{oc} and J_{sc} with the relative mean deviations of 13.2%. 22
3.13 Relative efficiency vs. series resistance R_s for two different R_r's. 23
3.14 (a) Schematic band diagram of CdS/CdTe cell showing the main junction and back barriers in the absorber layer (CdTe); V_m and V_B are the main junction potential drop and the back barrier height, respectively, the dotted vertical line shows the metallurgical junction (b) J-V characteristics and equivalent circuit for a photovoltaic device with a back barrier operating in the back diode regime composed of the main junction J-V characteristic (1) and leaky back diode J-V characteristic (2). 24
3.15 (a) Band diagram of the standard device absorber layer where the back contact is not very high and operates in the back diode regime. (b) Band diagram of a back barrier blocked absorber layer under short-circuit conditions. (c) Same under reach-through conditions, $V > V_{RT}$. (d) The corresponding J-V characteristic (RT) is shown in comparison with that of the standard device (with back barrier operating in the back diode regime (BD)). The solid line shows the J-V characteristics of a composite device consisting of the standard and reach-through devices in parallel. In the latter, the reach-through voltage (V_{RT}) appears to play the role of the open-circuit voltage when $V_{RT} < V_{oc}$. . 25
3.16 (a) Equivalent two-diode circuit (inset) and J-V characteristics of the reach-through micro-diode (shunting the current) and its more robust neighborhood (supplying the current). The reach-through micro-diode finds itself under forward bias and runs exponentially high forward current. (b) Current distribution in a system of robust diodes surrounding a reach-through diode. Fat arrow shows shunting current through the reach-through micro-diode, with polarity opposite to that of the photo-generated currents supplied by the majority of micro-diodes. L is the screening length. 29
3.17 "Bad back contact" J-V characteristics for a cell without interfacial layer (IFL) and similar cell with good back contact obtained by application of the IFL (designed in Ref. 37) prior the cell metallization. 33

3.18 "Bad back contact" J-V characteristics for a cell without interfacial layer (IFL) for different light intensities indicated in the figure. Note V_{oc} independent of light intensities and extremely large forward currents. Dashed line shows linear dependence in the space-charge-limited current region. 34
3.19 Ratios of the 1 sun to lower light intensity I currents versus voltage. The ratios are proportional to $1/I$ for the reverse current and space charge limited current regions. 35
4.20 Power-dependent photoluminescence on $2x10^{13}/cm^2$ Cu-implanted and annealed sample excited by 488 nm Ar laser. Broad peak at 1.47 eV shifts to higher energy with laser power. Dashed lines: peak of DAP transition obtained from deconvolution (centers of peaks are labeled); solid lines: data. 41
4.21 a)PL on undoped first quality CdTe wafer from Nikko Materials Co., Ltd with high quality, excited by 350 sun laser; b)PL on second quality CdTe wafer from Nikko Materials Co., Ltd and Keystone Crystal, excited by 100 sun 752nm lasers. 43
4.22 PL FROM annealed Cl-implanted CdTe wafer from Nikko Materials Co., Ltd , excited at 37 sun, 752nm. a) full spectrum; b) bound-exciton band shifting to lower energy as Cl dopant increases. 44
4.23 Experimental setup at MR-CAT. 46
4.24 XAFS spectra emphasizing on the XANES region. a) Non-chloride treated CdTe films with diffused copper show features similar to Cu2Te; b) chloride-treated CdTe films with diffused copper show features similar to Cu2O and CuO. 46
4.25 Fourier Transform of EXAFS. 47
4.26 a) Fourier Transform of $CdCl_2$ treated CdTe:Cu with long diffusion (ct070) and theoretical fitting; b) comparison of CdTe:Cu (ct070) with CuCl and $CuCl_2$. 49
4.27 Fourier transform of Cu K-edge EXAFS function. Fine lines: experimental data, thick lines: theoretical fitting. 50

List of Tables

2.1 Comparison of IV data of cells prepared with and without HR layer. 3

2.2 CdS/CdTe device data on SnO_2:F and ZnO:Al TCOs (NREL tested). 5

3.3 Experimental verification of main junction vs. back contact quality predictions 32

3.4 Reach-through microdiodes model predictions 36

4.5 FEFF fitting results on parameters of local structure around Cu atoms in different CdTe polycrystal films. Note: (1) $(Cu_2O)^*$, $(CuO)^*$ mean contribution from Cu-O bonds selected from Cu_2O or CuO crystal structure respectively; (2) All the other scattering paths arise from Cu-Cu and Cu-Te bonds selected from the Cu_2Te structure; (3) Since single scattering paths are the ones with strongest scattering magnitudes, we are presenting only single scattering paths obtained in the fitting and ignore other multiple scattering paths. For example, the path Cu-Te means an electron emitted from Cu atom is scattered back by the neighbor Te atom, and returns to the initial Cu atom. 51

1. INTRODUCTION

1.1. Background

The purpose of this subcontract, as part of the R&D Partners Category of the Thin Film Photovoltaics Partnerships Program (TFPPP) of NREL is to 1) extend research efforts on cell structure and fabrication mainly through the use of magnetron sputtering, including window and back contact buffer layers, alternative back contacts, and preparation of inverted cell structures; 2) perform CdTe-based cell modeling which goes beyond traditional numerical models to include electric potential and electric current distributions in cells, the effects of nonuniformities on cell and integrated module performance; 3) to extend efforts on materials and device characterization with emphases on the use of photoluminescence (PL), extended X-ray absorption fine structure (EXAFS), performed in parallel with current-voltage (I-V) and spectral quantum efficiency (SQE) device measurements; and 4) to support workforce development through the education and training of undergraduate, graduate, and postdoctoral students in the PV area.

This final report covers a three-year NREL thin-film partnership subcontract with the University of Toledo which has three task areas: 1) cell structure and fabrication, 2) cell modeling, and 3) characterization of materials and devices.

1.2. Objectives of this subcontract

The primary objectives of this research by this subcontractor as an R&D partner is to address fundamental issues especially related to:

- enhancing the total-area, thin-film cell efficiency through magnetron sputtering of novel materials and alloys,
- improving the understanding of nonuniformities and their impact on device and module performance through novel experiments and modeling,
- improving the understanding of the materials and devices through the use of photoluminescence (PL), capacitance-voltage (CV), Hall, Raman, absorption, scanning electron microscopy (SEM) with energy dispersive x-ray spectroscopy (EDS), and X-ray absorption fine structure (XAFS),

- identifying materials and structural issues that can lead to improved cell stability, including buffer and interfacial layers and novel back contacts,
- identifying novel device structures to find pathways for reducing the utilization of CdTe, and development of substrate CdTe structures for comparison with standard superstrate devices and to determine possibilities for roll-to-roll manufacturing, and
- strengthening the thin-film PV infrastructure through education and training of undergraduate and graduate students as well as postdoctoral associates.

1.3. Technical approach

The scope of work under this subcontract is divided into three primary efforts which are reflected in the three following Sections. The first effort is focused on the use of magnetron sputtering for fabrication of CdTe-based cell structures. This includes the use of interfacial layers in sputtered cell structures and the fabrication of (inverted structure) substrate cells on metal or metal-coated glass substrates. The second effort is focused on cell modeling. We seek to model quantitatively the effects of two-dimensional non-uniformities in electric potentials and current distributions in thin-film CdTe cells and integrated modules, including the effects of buffer, absorber, and window layer parameters. The modeling effort includes comparison with cell and materials measurements, such as described in the third effort. The third effort is focused on the characterization of CdTe-based PV materials and devices. This effort includes studies of photoluminescence (PL) and electroluminescence (EL) of magnetron-sputtered (MS) and vapor-transport-deposited (VTD) materials and cells before and after stressing. The effort also includes small-spot PL (PL mapping) on standard cells and bias-dependent PL for direct comparison with the cell modeling efforts. We also have performed Hall, x-ray diffraction, Raman, SEM, capacitance-voltage, and synchrotron x-ray absorption studies on these materials.

2. CELL STRUCTURE AND FABRICATION

2.1. CdS/CdTe Devices with a ZnO High Resistivity Buffer Layer

In our earlier annual report (2001-02),[1] we studied the sputtered CdTe cells prepared on SnO_2:F high resistivity (HR) layer obtained from First Solar. It was observed that the performance of cells depends on 1) the fabrication temperature and process conditions of the HR layer, 2) the post-deposition heat treatment, 3) the deposition temperature of CdS and 4) the deposition method used for CdS and CdTe layers. We observed also the variation in HR properties. Since, we obtained high efficiency for sputtered CdTe cells using a heavily doped ZnO:Al as the front contact TCO,[1–3] we started developing a ZnO HR buffer layer at UT. Initially, we tried to deposit HR ZnO by reactive sputtering from an intrinsic ZnO target in Ar/O_2 ambient, but it was difficult to control the desired sheet resistance of the film. Secondly, considered that using a bilayer front contact i.e. conducting ZnO:Al/ intrinsic HR ZnO, might lead to out-diffusion of Al from the conducting ZnO:Al into intrinsic HR ZnO, especially during post-deposition heat treatment or long-term stability testing. This could reduce/eliminate the effect of the HR layer. Therefore, we optimized the conditions for deposition of the HR buffer layer from a ZnO:Al (2% Al_2O_3) target in Ar/O_2 ambient. The desired sheet resistance of 0.1 to 0.12 μm thick film was about 10^4 Ω/sq.

Sample ID	HR layer	CdS (μm)	V_{oc} (mV)	J_{sc} (mA/cm^2)	FF %	Efficiency %	R_s (ohm-cm)	R_{sh} (ohm-cm)	Aver # of cells
T927A	-	0.08	700	21.77	67.28	10.25	6.31	895	9/9
T928A	-	0.13	810	20.15	68.21	11.13	7.97	1556	7/9
H923A	SnO_2	0.08	782	22.71	68.46	12.16	6.3	728	9/9
H924A	SnO_2	0.13	827	20.75	70.07	12.01	5.23	1085	9/9
196A2	ZnO	0.08	806	23.3	67.92	12.75	10.45	618	3/9

Table 2.1: Comparison of IV data of cells prepared with and without HR layer.

During the initial stage of experiments, the ZnO HR layer was deposited on a conducting SnO_2:F layer (TEC-7) on a 3mm glass substrate. In our TFPPP project annual report of 2001,[1] we presented the IV and QE performance data of CdTe cells made with a range of CdS thickness. We reported that the average V_{oc} of cells (made *without* using HR layer)

decreased from 810 mV to 700 mV for the reduction in CdS thickness from 0.13 μm to 0.08 μm, while the cells made *with* an SnO_2 HR layer did not show so much drop in V_{oc}. Therefore, to compare the performance with earlier cell having as SnO_2 HR layer, the present cells were made on TEC-7/ZnO:Al HR substrates with 0.08 μm CdS and 2.3 μm CdTe films deposited using standard sputtering parameters. The cells were finished with our standard Cu/Au back contact. Table 2.1 shows the IV performance data of the cells. The data is average of up to 9 cells. For comparison, the detailed IV performance data of cells with and without the SnO_2 HR layer are also shown in Table 2.1. The V_{oc} of the cell with the ZnO HR layer (196A2) is higher than that of the cell without HR (T927A) made with 0.08 μm CdS. It is slightly higher than the cell with the SnO_2 HR (H923A) made with 0.08 μm CdS, and the cell without HR layer (T928A) made with thicker CdS (0.13 μm). This shows that the sputtered ZnO HR layer works suitably with sputtered cells.

Figure 2.1 shows the comparison of external quantum efficiency of the best cells prepared with SnO_2 or ZnO HR layers. The cell with the ZnO HR layer shows slightly higher QE in lower wavelength and slightly lower QE in longer wavelength region. This could be due to interdiffusion across the ZnO/CdS interface during processing similar to that reported between the Zn_2SnO_4/CdS [4]. To understand this interdiffusion, experiments with annealed ZnO/CdS are in progress.

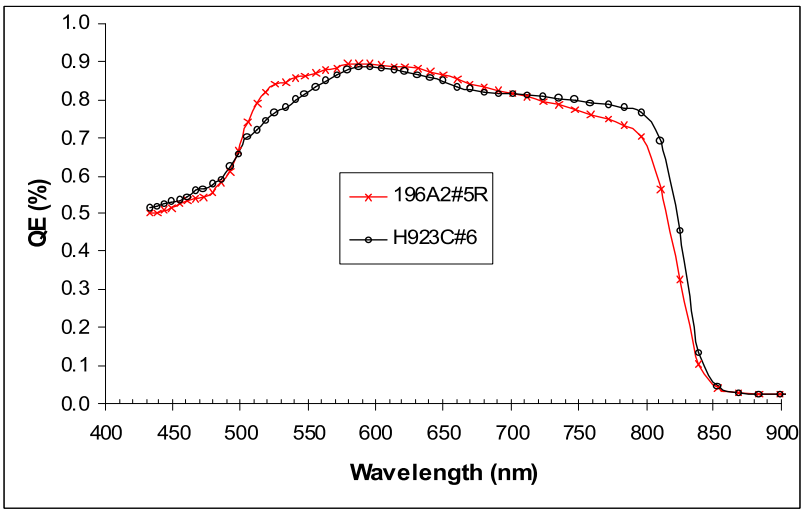

Figure 2.1: External quantum efficiency of best cells prepared on SnO_2 and ZnO HR layers.

2.2. Sputtered ZnO:Al Layer as the Front Contact TCO

In our 2001-02 annual report,[1] we demonstrated successfully the use of heavily doped ZnO:Al layer as the front contact TCO in CdTe solar cells, and achieved 14% efficiency (NREL tested). We have compared the electrical and optical properties of in-house deposited ZnO:Al and commercial SnO_2:F TCOs. Also, we compared the relative stability performances of sputtered CdS/CdTe cells prepared on SnO_2:F or ZnO:Al under one-sun light soak at V_{oc}. Most of these results have been published,[1–3] therefore we report here only highlights of the results.

ZnO:Al films were deposited using RF magnetron sputtering from a ceramic ZnO:Al_2O_3 (2%) target at 220 ^{o}C on 1 mm thick aluminosilicate (ASG) in pure argon gas at 48 W of RF power and 10-12 mTorr pressure. The ZnO:Al film showed ∼95% average transmission in the visible region, higher than that of SnO_2:F film by an average ∼5%. Although both center and edge areas of ZnO:Al films showed similar optical properties in visible region, the edge area showed higher transmittance and lower absorbance in near-IR region. This is an indication of higher mobility in the edge area which would be advantageous for the fabrication of bottom cells in tandem-junction devices. A comparison of ZnO:Al on 1mm thick sodalime glass (SLG) and SnO_2:F films on 3mm SLG (commercial product of Pilkington which is routinely used) showed more absorbance, reflectance and less transmittance (by ∼12%) in the visible region for SnO_2:F films. The ZnO:Al film is more transparent over the whole spectrum.

TCO/ Performance	V_{oc} (mV)	J_{sc} (mA/cm^2)	FF (%)	Efficiency (%)	Series Resistance (ohm*cm^2)	Shunt Resistance (ohm*cm^2)
SnO_2:F	820	20.7	73.96	12.6	3.9	1822
ZnO:Al	814	23.6	73.25	14.0	3.16	989

Table 2.2: CdS/CdTe device data on SnO_2:F and ZnO:Al TCOs (NREL tested).

The electrical properties of ZnO:Al/ASG and SnO_2:F/SLG structures were determined using Hall measurements. While the optical measurements showed differences in transmission and absorption between center and edge area, the Hall measurement showed almost the same mobility and carrier concentration. The difference in results from the two measurement

techniques could be due to the fact that Hall technique measures bulk, in-plane transport properties, in which the effect of grain boundaries can be important. Optical measurements, by contrast, measure microscopic bulk properties in which grain-boundary scattering is of secondary importance. The hall mobility and carrier density for ZnO:Al and SnO_2:F are $\sim$40 $cm^2/V*s$ and $4x10^{20}$ cm^{-3}, and 22 $cm^2/V*s$ and $8x10^{20}$ cm^{-3}, respectively. The better optical and electrical properties of ZnO:Al would be beneficial in the manufacturing of monolithically interconnected solar modules to allow increasing the cell width, and hence decreasing the dead area due to scribing. This would increase the power per unit area of the modules.

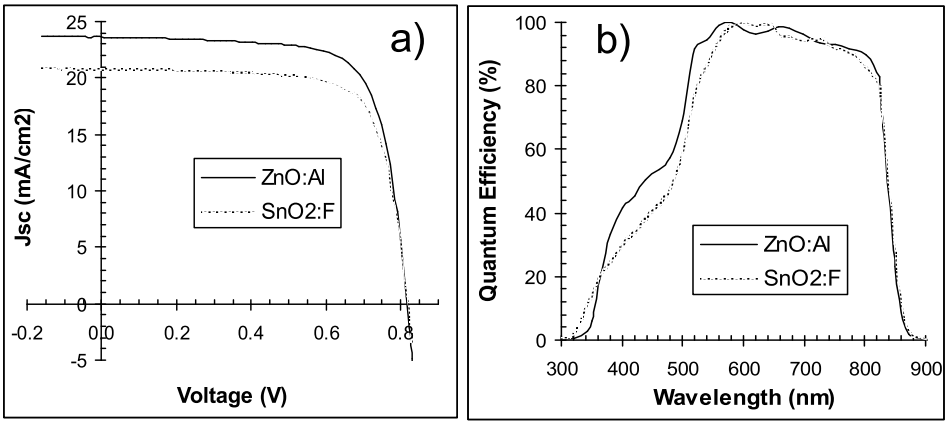

Figure 2.2: I-V and QE plots of CdS/CdTe solar cell on ZnO:Al and SnO_2 TCO.

The CdS/CdTe solar cells were fabricated by deposition of 0.13 μm thick CdS and 2.3 μm CdTe layers using RF magnetron sputtering on as-deposited ZnO:Al/ASG (1mm) or SnO_2:F/sodalime glass (3mm). The deposited structures were treated in vapors of $CdCl_2$ at 387 ^oC in dry air. The devices were completed with evaporation of a Cu/Au back contact (without any treatment of the CdTe surface). Table 2.2 shows the cell performance data obtained at NREL. Figure 2.2 shows the comparison in current-voltage and quantum efficiency for the cells on both type of TCOs. While the V_{oc} and FF are almost the same for both devices, the ZnO:Al based device showed an improvement in J_{sc} by 15%. The efficiency of the device increased from 12.6% to 14.0% entirely due to increased J_{sc} because of lower sheet resistance and higher transmission of the glass/ZnO:Al in visible region. The effect of low sheet resistance is clearly shown by the lower series resistance of the cell on ZnO:Al. To the best of our knowledge, this is the highest efficiency ever reported using ZnO:Al as

the front contact to a superstrate CdS/CdTe cell. It is also the highest efficiency for an all-sputtered CdS/CdTe solar cell.

Figure 2.2b shows the quantum efficiency of the best devices prepared on both types of TCOs. The QE of the ZnO:Al-based device is lower in the 300-340 nm region due to lower bandgap of ZnO:Al in comparison to SnO_2:F TCO. The figure clearly shows that the ZnO:Al-based cell has higher collection in the blue region (360-560nm) even though the deposited CdS was 0.13 μm in both cases. The QE in the longer wavelength region (820-860 nm) shows the absorption edge of the modified absorber, CdTe1-xSx, obtained due to interdiffusion of some CdS into CdTe during $CdCl_2$ treatment. The similar response in this region indicates that CdS diffusion is similar in both cases, and therefore the higher QE response in the blue region is truly due to better transmission of the TCO/ASG. However, the ZnO:Al/CdS interface could also have been modified during the CdCl2 treatment because of some interdiffusion of Zn into CdS, increasing the bandgap and transmittance of CdS similar to interdiffusion between the Zn_2SnO_4/CdS interface,[4] and hence contributing in enhanced photo-response in the 400 to 500 nm region. The higher QE response (by $\sim$11%) of the ZnO:Al based device in the visible region (550-825 nm) is clearly due to better transparency of ZnO:Al TCO in the visible region.

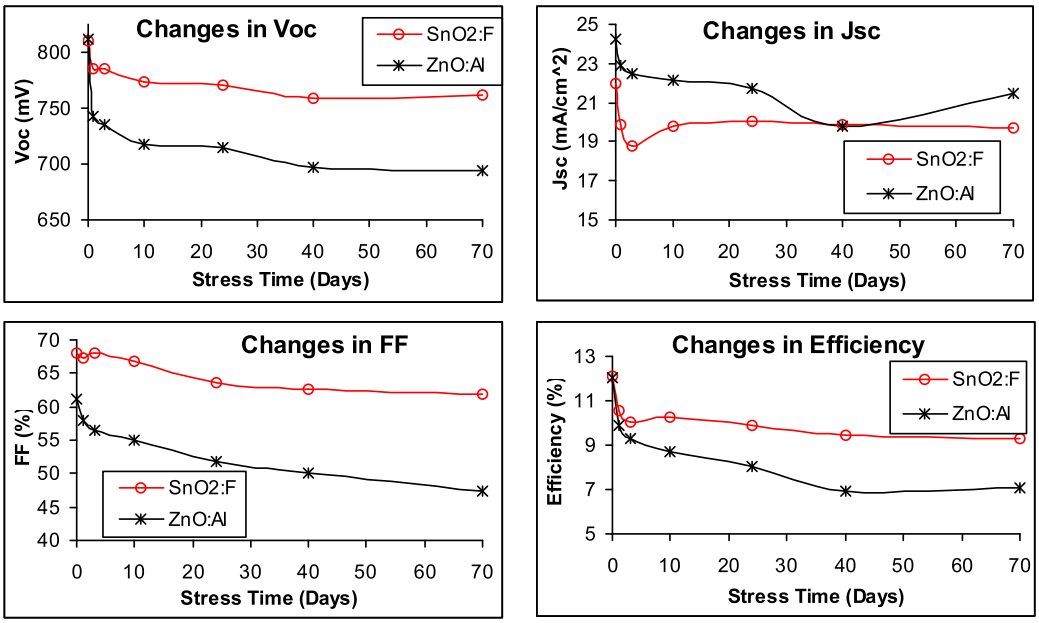

Figure 2.3: Changes in V_{oc}, FF, J_{sc} and efficiency with light soak time.

The CdS/CdTe devices on both types of TCOs were light soaked side by side under one-sun simulated illumination. The devices were kept at open circuit condition at ∼55 ^{o}C. The samples were taken out at intermediate intervals and measured for I-V performance at the University of Toledo after cooling down to room temperature for ∼30 min. The data of Figure 2.3 are a 7-10 cell average of the changes in V_{oc}, J_{sc}, FF and efficiency with light-soak time. The light soak triggered different degradation mechanisms for the two types of TCOs. For the ZnO:Al based device, V_{oc}, J_{sc} and FF degraded by 9.5, 7.2 and 7.8% leading to degradation in efficiency by 22.6% in the first three days of stressing. For the SnO_2:F based device FF and V_{oc} degraded by only 0.22 and 3%, large degradation occurred in J_{sc} (by 14.5%) leading to overall efficiency decrease by 17% for the same duration of light soak. The initial fast degradation in ZnO:Al-based devices caused a final degradation in efficiency by 41.5% which is almost double the degradation (23.0%) in efficiency of the SnO_2:F-based devices for the same duration of light soak. The initial fast degradation in ZnO:Al based devices could be due to its lower thermal stability and/or interdiffusion across the ZnO/CdS interface during processing and light soaking.

Conclusion ZnO:Al films on aluminosilicate glass were successfully used to fabricate a 14% CdS/CdTe solar cell without using an anti-reflection coating, a high resistivity buffer layer, or thinning the CdS layer. The improvement in efficiency was mainly due to better glass transmission, and to lower sheet resistance and higher transmission of the ZnO:Al TCO which increased the short-circuit current density by 15%. We believe that the 14% cell efficiency is the highest ever reported using a ZnO:Al front contact, and also the highest for any CdS/CdTe solar cell in which all semiconductor layers are prepared by sputtering. This result confirms that the moderate temperatures needed for the magnetron sputtering process can provide important advantages in cell fabrication and expand the range of materials available for thin-film polycrystalline solar cells. In comparison to sputtered cells on commercial SnO_2:F, the stability of these initial ZnO:Al-based cells is poorer, however. This may be due to interdiffusion across the ZnO:Al/CdS interface and the absence of a buffer layer.

2.3. Work in progress

The effect of annealing of ZnO:Al/CdS on performance and stability of completed cells is being carried out to confirm the interdiffusion effect and to improve the performance. A high resistivity ZnO buffer layer on conducting ZnO:Al is also being used together with a thinner CdS layer to increase the photo-current.

References

[1] Alvin D. Compaan et al., "The fabrication and physics of high efficiency CdTe thin film solar cells", annual technical report for the period Sep. 2001 to Aug. 2002, NREL contract No. NDJ-1-30630-02.

[2] Akhlesh Gupta and Alvin D. Compaan, "14% CdS/CdTe solar cell with ZnO:Al TCO" Compound Semiconductor Photovoltaics, edited by Rommel Noufi, William N. Shafarman, David Cahen and Lars Stolt, Mat. Res. Soc. Symp. Proc. **763**, 161 (2003).

[3] Akhlesh Gupta and Alvin D. Compaan, "All sputtered 14% CdS/CdTe thin-film solar cell with ZnO:Al transparent conducting oxide" *Appl. Phys. Lett.*, **85**, 684 (2004).

[4] X. Wu, R. Ribelin, R.G. Dhere, D.S. Alvin, T.A. Gassert, S. Asher, D.H. Levi, A. Mason, H.R. Moutinho and P. Sheldon, Proc. Of 28th IEEE Photovoltaic Specialists Conference, Anchorage, Alaska, Sep. 17-22, 470 (2000).

3. CELL MODELING

3.1. Overview

This section will summarize the results of modeling part of this project including some of two previous annual reports and the present one. At a very general level, we want to highlight two such results

1. We have understood and described the role of lateral nonuniformities in thin film photovoltaics. Based on our present estimates, the nonuniformity loss in commercial integrated modules can be as large as $\sim 30\%$, and nonuniform degradation can be by the order of magnitude faster than that of more uniform devices.

2. We have proposed and experimentally proven a new physical model of CdTe photovoltaics, which we believe is a MIS device as opposed to the commonly used model of p-n device. This has numerous practical consequences, one of which a simple recipe of stable Cu-free device with the efficiency of 13%.

More specifically, our results supporting the first item are as follows (some from "Characterization" task area):

- Concept of and equation for the screening length describing how far a local nonuniformity extends its detrimental effects for a given set of parameters: light intensity, nonuniformity amplitude, and TCO sheet resistance.[1,2]

- Software for numerical modeling of nonuniform solar cells.[1]

- Nonuniform degradation of solar cells.[1]

- Statistics of fluctuations of the main photovoltaic parameters; low-light diagnostics of lateral nonuniformities in solar cells.[2]

- PL mapping and related mappings by other techniques from other groups.[1,2]

- Thermography diagnostics and modeling.[2]

- Pspice modeling of integrated interconnect modules.

- Self-healing electrolyte treatments ("red wine effect") mitigating nonuniformity effects.[2]

Our results supporting the second item are as follows:

- Properly deposited buffer layer leads to high V_{oc} devices without Cu doping.
- Properly deposited buffer layer can create interface states that deplete CdS enough to make TCO coupling with CdTe in the manner of MIS device.
- High back barrier switches the cell into the "reach-through" regime, where it does not generate any current at voltages lower than certain threshold voltage.
- Local "reach-through" regions dramatically decrease the device V_{oc}.
- Cold evaporated gold contact in combination with our invented aniline treatment makes a stable back contact without Cu doping.
- The Cu-free stable device recipe is TCO/buffer/CdS/CdTe/aniline(IFL)/Au without final heat treatment.

In what follows we describe our latest findings not covered in previous annual reports.

3.2. Reach-through band bending in semiconductor thin films

The phenomenon of Schottky barrier formation is well known from standard junction theory. Here we introduce a new scenario of junction formation for semiconductor thin films where the Schottky barrier is absent or strongly suppressed. The underlying idea is that in a thin film semiconductor the Fermi level (F) can be shifted by generating a limited number of defects. Such a scenario becomes impossible for a thick semiconductor where F is fixed by the bulk.

We consider a three-component system of a thin n-type semiconductor film sandwiched between a metal and p-type semiconductor. Both system interfaces can have interfacial states. In our experimental verification this is represented by an n-type CdS film between a conductive electrode and p-type CdTe, which combination has important photovoltaic applications.[4] Its band diagram is shown in Fig. 3.4 for a particular case where the Fermi

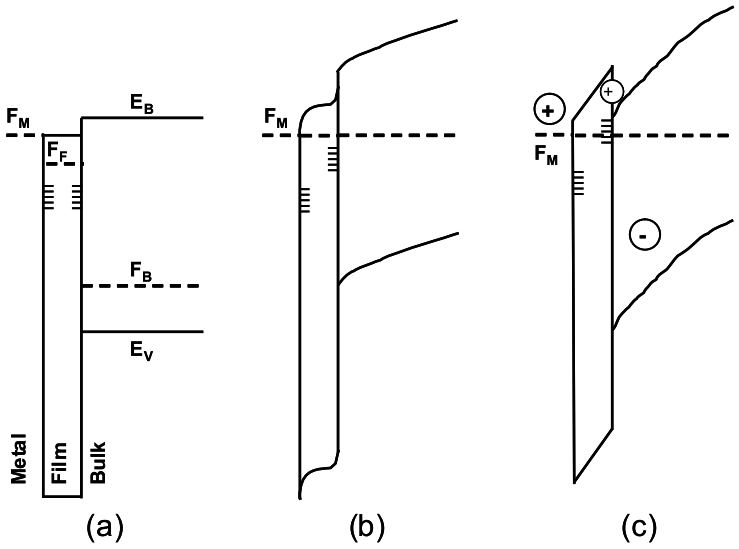

Figure 3.4: Energy-band diagrams for a system of metal, semiconductor thin-film, bulk semiconductor (a) before contact, (b) after contact as predicted by the standard Schottky barrier formation scenario, (c) after contact accompanied by acceptor defect generation.

energies F_F and F_B in the film and bulk semiconductor components are close, while being significantly different from that of the metal (F_M). We assume that the screening length in the n-type semiconductor forming the film is considerably shorter than the film thickness, $L \ll l$. For such a system, the standard junction theory predicts a weak p-n junction between bulk and thin film semiconductors and a strong Schottky barrier between the metal and the film [Fig. 3.4(b)].

A conceivable effect of lowering F_F shown next in Fig. 3.4(c) is due to acceptor defect generation. As a result, the film becomes depleted and strongly increases its screening length, $L \gg l$. The metal and bulk semiconductor then interact across the film similar to MIS structures, and align their Fermi levels, $F_B = F_M$. In particular, the band bending appears at the film interface opposite to the metal as though the latter was in direct contact with the bulk semiconductor. We call this new phenomenon a reach-through band bending. When strong, it results in an inverse layer in the bulk semiconductor.

Phenomenologically, the film depletion corresponds to a potential barrier in the band diagram. The barrier is needed to separate the conduction band from the Fermi level and thus to self-consistently maintain the film insulating properties [as schematically shown in Fig. 3.4(c)]. Such a barrier is achieved by shifting up the entire thin-film energy spectrum

in the process of aligning of its lowered Fermi level with F_M.

As usual, the barrier in the electric potential corresponds to a certain electric charge distribution related to the defect and interfacial state parameters. In turns, the latter determine the barrier shape and height. As a conceivable example, we note that lowering F_F empties interfacial states thus making interfaces charged positively. This results in the charge distribution shown in Fig. 3.4(c). The CdS interior region can pick some electric charge too, which depends on the material density of states and will not be further discussed here.

As a numerical example related to the data below, we assume a typical interfacial state density $\sigma \sim 10^{11} - 10^{12}$ cm^{-2} and film thickness $l \sim 10^{-5}$ cm. This results in the barrier height $V_B \sim (4\pi/\epsilon)\sigma q^2 l \sim 0.1 - 1$ eV, where q is the electron charge and ϵ is the dielectric constant.

Consider more quantitatively the energy balance for the diagram in Fig. 3.4(c). nL electrons per unit area move to the bulk semiconductor gaining the energy $\Delta F_{MB} \equiv F_M - F_B$ each, and occupying the region of width L with screening charge density n in the bulk semiconductor. This increases the electrostatic energy in both the film and bulk semiconductor (second and third terms on the right hand side of Eq. (3.1) below). Also, we add the defect generation energy W_d that depends on defect chemistry in the film and semiconductor. Optimizing the total energy

$$W(L) = -nL\Delta F_{MB} + \frac{2\pi n^2 q^2 L^3}{3\epsilon} + \frac{2\pi n^2 q^2 L^2 l}{\epsilon} + W_d \tag{3.1}$$

yields the the barrier width L_l and energy gain $W(L_l)$,

$$L_l = \sqrt{L_0^2 + l^2} - l, \quad L_0 \equiv \sqrt{\frac{\epsilon \Delta F_{MB}}{2\pi n q^2}}; \tag{3.2}$$

$$W(L_l) = -\frac{2nL_l\Delta F_{MB}}{3}\left(1 - \frac{lL_l}{2L_0^2}\right) + W_d. \tag{3.3}$$

For the case of $l = 0$ our consideration reproduces the well-known result[6] for a Schottky barrier. The scenario of Fig. 3.4(c) becomes energetically favorable when $W(L_l)$ is lower than the energy $W(L_0)$ calculated with the parameters corresponding to the thin film (with $\Delta F_{MB} \to \Delta F_{MF} \equiv F_M - F_F$). As is seen from Eq. (3.3), such a scenario is more likely when $l \ll L_0$.

As exposed to the absorbed light, a strong reach-through band bending can generate a high open-circuit voltage, thus paving a way to efficient photovoltaics. A related conceiv-

able effect is that shifting up the thin film energy spectrum can affect the electron-hole recombination and further improve the system characteristics.

We now turn to the experimental verification of the above scenario and note preliminarily that the suggested defects can be introduced through either surface states on the interface between the thin film and the metal or by chemical doping. Our experiments were aimed at revealing similarities between the effects of surface modification and doping.

As an implementation of a structure in Fig. 3.4, we used a 0.25 μm thick n-type CdS and 3.5 μm thick p-type CdTe deposited on a glass substrate by close-space sublimation (see Ref. 3). Their respective charge carrier concentrations,[5] $n \sim 10^{17}$ cm^{-3} and $p \sim 10^{14}$ cm^{-3}, were such that the CdS film thickness $l = 0.25$ μm was much smaller than the screening length in CdTe and much larger than that in CdS ($L_0 \sim 3$ μm and $L_0 \sim 0.1$ μm, respectively, assuming a built-in voltage ~ 1 V[6]).The transparent conductive oxide (TCO) layer of sheet resistance 15 $\Omega/\Box$ on a glass substrate underlying the CdS was used as a conductor. The structures underwent the standard anneal in the presence of $CdCl_2$ vapors known to improve electrical characteristics.[7]

To affect the CdS interface, we additionally deposited on the TCO a 0.1 μm thick tin-oxide based buffer layer[8,9]. Its sheet resistance ($\approx 1.2 \cdot 10^4 \Omega/\Box$) was much higher than that of the TCO, yet low enough to consider it a metal in the sense that its Fermi level is above that of the CdS film (as assumed in Fig. 3.4 where the leftmost parts of the diagrams can represent either the TCO or the buffer layer).

For the alternative CdS modification by doping, Cu was introduced at the metal semiconductor junction through an anneal step.[10] The latter procedure promotes the movement of Cu to the CdS film where it accumulates in high concentrations.[11]

We have measured current-voltage (J-V), quantum efficiency (QE) and capacitance-voltage (C-V) characteristics that constitute the basic diagnostics for CdS/CdTe photovoltaics.[4] The J-V results in Fig. 3.5 represent the averages of 10 1.1 cm^2 area cells. QE (measured with white bias light; Fig. 3.6) and CV (at 75 kHz; Fig. 3.7) measurement were taken on 2 cells for each condition.

Both the open-circuit voltage and short-circuit current (under one-sun light intensity) in Fig. 3.5 are almost the same in the range of practically significant values for the undoped devices with buffer layer and for doped devices without buffer layer. However, these parameters are much lower when neither buffer layer nor Cu doping are present. This shows that

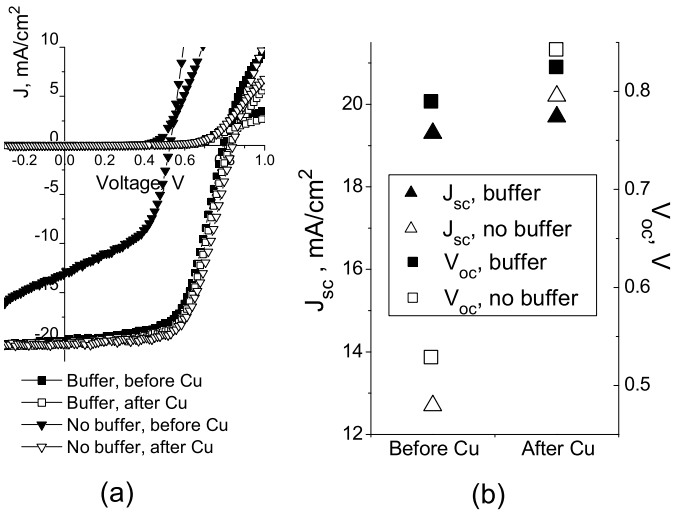

Figure 3.5: J-V curves (a) and Open circuit voltage (V_{oc}) and short-circuit current (J_{sc}) (b) for Cu doped and undoped CdS/CdTe structures with and without buffer layer.

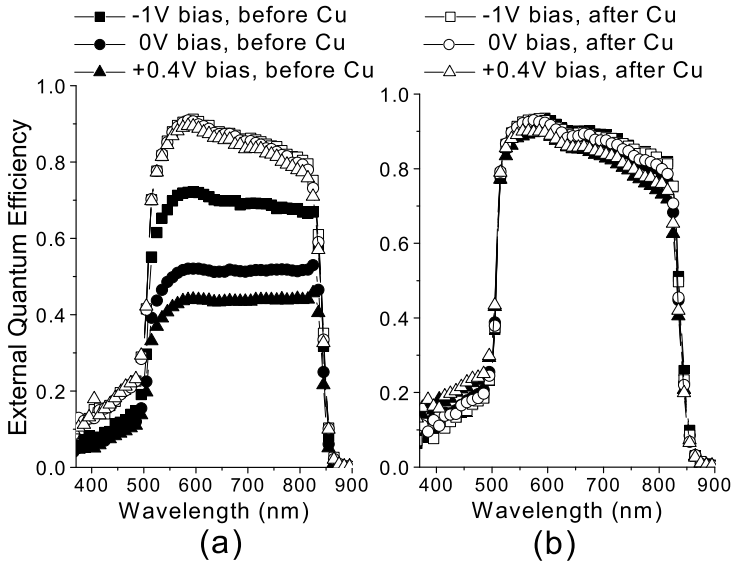

Figure 3.6: QE characteristics of CdS/CdTe structures without (a) and with (b) buffer layer for different voltages before and after Cu diffusion.

either the buffer layer application or Cu doping lead to a well developed junction where the built-in field is strong enough to provide efficient current collection.

Furthermore, the close numerical coincidence between the two recipe results suggest that Cu and the buffer layer have a similar effect on the CdS layer. Since Cu is known to act

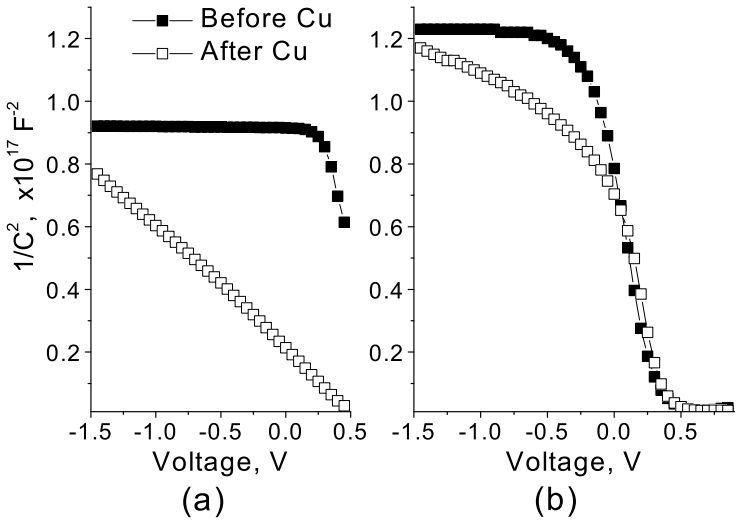

Figure 3.7: C-V characteristics of CdS/CdTe structures without (a) and with (b) buffer layer before and after Cu diffusion. In the graph (a) the data are truncated to $V < 0.5$ V to avoid the conduction contribution indicated by the phase angle between the real and imaginary parts of the measured admittance.

as an acceptor in CdS,[12] Fig. 3.4(c) seems to represent a plausible band diagram for either the Cu-doped or the buffer-layer-containing structure. This choice is additionally supported by the observation (Fig. 3.5(a)) that the dark J-V curves are abnormally flat thus showing extremely high series resistance. We attribute the latter to a barrier V_B in Fig. 3.4(c) (which is photoconductive; similar to Ref. 13). The undoped devices without buffer layer are better described by the diagram in Fig. 3.4(b), which predicts a poorly developed junction and thus low V_{oc} and J_{sc}.

QE data (Fig. 3.6) confirm our interpretation. Since QE represents the number of electron-hole pairs collected per photon, we conclude that carrier collection is equally improved by doping or applying a buffer layer. In addition, the QE of undoped structures without buffer layer are strongly bias-dependent. This means, again in agreement with Fig. 3.4(b), that the junction is not well developed and thus carrier collection can be considerably improved by reverse bias. Disappearance of such bias dependence after Cu diffusion can be attributed to the formation of a well developed junction. A strong junction consistent with the diagram in Fig. 3.4(c) is also evident from the QE data for the structures with buffer layer. Similarly to the J-V characteristics, the QEs remain practically insensitive to Cu

doping for the buffer layer containing structures, meaning that the junction once developed by the buffer layer effect remains practically insensitive to further material compensation, consistent with the above understanding.

C-V data (Fig. 3.7) add specificity to the above interpretation. Samples without buffer layer and Cu show voltage-independent geometrical capacitance. Cu-doping creates a space charge region, which, in accordance with the standard interpretation,[6] is responsible for the slope of C^{-2} vs. V. However, with the J-V data in mind, that region does not seem to contribute much to the device barrier height (close similarity between the Cu and buffer layer effects). Finally, the buffer-layer-containing devices exhibit C-V characteristics typical of MIS structures with C varying between two limiting geometrically related values,[6] which, again, is consistent with the diagram in Fig. 3.4(c). Also, the latter is consistent with the observed potential drop between the CdS and buffer layer in the buffer/CdS/CdTe structure studied with the Kelvin probe technique.[14]

We conclude that the above data confirm the hypothesis of Schottky barrier suppression in a semiconductor thin film and show that the metal can act through the film causing reach-through band bending. More specifically, our findings suggest that surface treatments can dramatically change the dielectric properties of a thin film and thus affect the electric field distribution in the entire system. For example, the CdS deposition method (sublimation or sputtering) and temperature can affect the device V_{oc}, a prediction that can be verified experimentally.

3.3. Modeling of non-uniformity losses in integrated large-area solar cell modules

Low-cost large-area photovoltaic modules are produced as either polycrystalline or amorphous thin films, which are intrinsically nonuniform. If we imagine a large area PV module as a set of interconnected small area cells, then non-uniformity will result in variations between photovoltaic parameters of such cells.[15,16] In particular, occasional faulty parts will affect the whole device performance leading to the output power loss and a distribution of parameters between commercially produced nominally identical modules.[17–19]

Even when there are no particularly faulty elements, connecting cells with different PV parameters in a circuit will result in a mismatch loss (quantitatively, a difference between the total power available from individual cells and the resulting measured power after intercon-

nection). In a typical PV module thousands of cells with randomly distributed parameters form a complex network combining parallel and in-series connections (see below). Estimate of non-uniformity related loss becomes then a non-trivial theoretical problem, further complicated by the effects of cell and interconnect resistances. A straightforward power loss characterization, either real or numerical, would be measuring a module power output and comparing it to the integral power generated by its constituting individual cells. It is implemented here based on a commercially available circuit design software PSpice.

PSpice was used in PV engineering,[20] mostly for numerical modelling of PV arrays. At the module level, the nonuniformity modelling concentrated on spatial variations in the irradiance level (hot spots and shadowing) and related current and stability losses.[21–23]

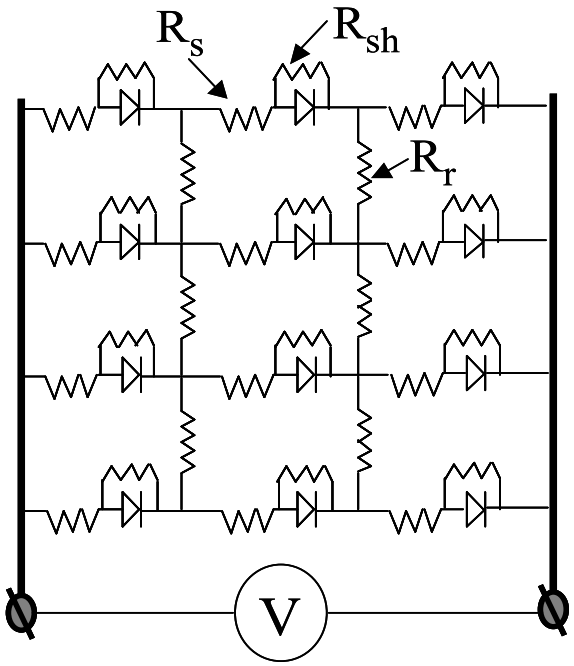

Figure 3.8: Random diode array with lump parameters: row (scribe) resistance R_r, series resistance R_s, and shunt resistance R_{sh}. Fat lines represent electrodes (bus bars) used to measure the system current and voltage.

Here we assume the irradiance uniform and consider variations in the electrical parameters of individual cells constituting the module. We address the following questions. What is the nature of the nonuniformity related loss, its statistical and topological characteristics? In particular, which fluctuations underlie the typical distributions of efficiencies of nominally

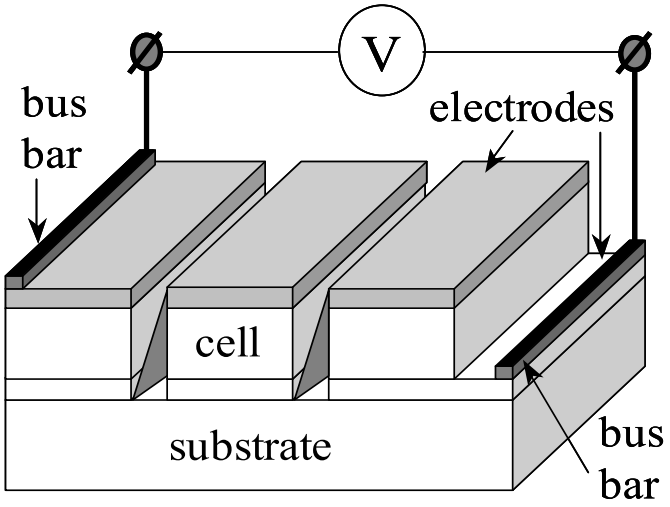

Figure 3.9: Sketch of integrated photovoltaic module on a monolithic (typically glass) substrate. Tilted fragments between cells represent interconnections through scribes.

identical production PV modules? What is the magnitude of the mismatch loss in a large area PV module?

Equivalent circuit In a typical large-area PV module many linear cells are connected in series.[4] The interconnects are made by monolithic integration via "scribe lines" (Fig.3.8), which do not set any tangible resistance between the cells. However, the typical length of linear cell, of the order of tens of centimeters, can be large enough to make its different parts electrically disconnected. To account for intra-cell nonuniformities one has to use the equivalent circuit where a linear cell is divided into a set of small dot-cells, whose linear size is smaller than the characteristic length L, over which the electric potential in a linear cell can change noticeably. The latter can be estimated based on the well-known formula for the telegraph line, $L = a\sqrt{R_r/R_{TCO}}$ where $a \sim 1$ cm is the cell width, R_{TCO} is its transversal resistance per length (equal to the TCO sheet resistance, $R_{TCO} \sim 10\Omega$) and $R_r \sim 1\Omega$ is its longitudinal (along the scribes) per unit length. This yields $L \sim 3$ cm, based on which we use dot cells of 1 by 1 cm connected in a circuit as sketched in Fig.3.9, where each diode represents a photodiode and is characterized its standard PV parameters, open-circuit voltage V_{oc}, short-circuit current J_{sc}, series resistance R_s, and shunt resistance R_{sh}.

We used PSpice software to model a circuit of 58 linear cells connected in series with each cell divided in 28 dot-cells, corresponding to a module of 2 by 1 ft with dot-cell area of 1 cm^2. V_{oc} for each cell was defined in terms of PSpice variables, saturation current J_0 and emission coefficient N. Each cell was assigned a set of random parameters, whose distributions were supplied to the program through modification of the "netlist" file. For each distribution, the integral module current-voltage (J-V) characteristic was obtained and compared to that of the uniform module with dot-cell parameters equal to the averages over the corresponding non-uniform distributions. We used the relative efficiency $\eta_{rel} = \eta_{nouniform}/\eta_{uniform}$ as a figure of merit to characterize the nonuniformity loss.

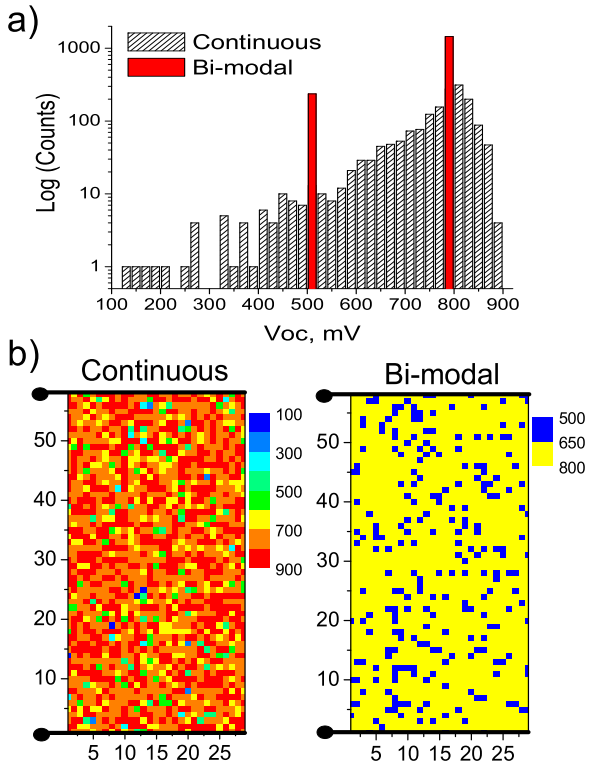

Figure 3.10: Disorder in V_{oc}. a) Generated statistical V_{oc} distributions - continuous and bi-modal (note the log scale), with the same average value $< V_{oc} >$=755 mV, standard deviation SD=100, relative dispersion $\delta = 13\%$; b) Maps of 29 by 58 diodes illustrate topological realization for corresponding statistical distributions. Relative efficiency $\eta_{rel} = 0.92$ is the same in both cases.

Results Statistics vs. geometry. A set of N random cells can be arranged into module in a great number $N! \gg 1$ of geometrically different ways. A nontrivial (even

counterintuitive) result of this work is that the geometry plays almost no role when $N \gg 1$ and the two first momenta of the statistical distribution of random parameters suffice to give a good description of nonuniformity loss. The underlying modelling results, are as following.

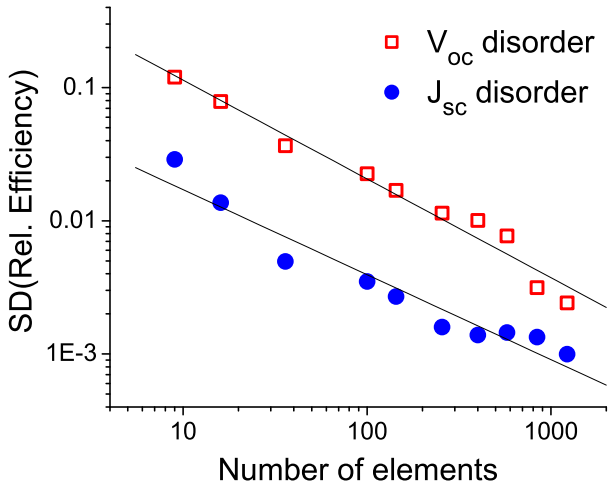

Figure 3.11: Standard deviation (SD) changes almost by 2 orders of magnitude from the smallest to the largest module (note a log-log scale). The cases of fluctuating V_{oc} and J_{sc} are shown. Straight lines represent linear fits.

A typical measured V_{oc} distribution was a superposition of a Gaussian and a long low-value tail (Fig.3.10a). We have found that, to the accuracy better than 0.1%, a module relative efficiency is independent of the distribution geometrical implementation when its average and dispersion remain fixed. We then made simulations for a markedly different bimodal distribution with the same average and dispersion. Again, to a high accuracy, our simulations gave the same result. We have verified then that the latter surprising result holds for large number of elements $N \gg 1$ and that the fewer N the stronger effect of geometry.

Scaling and mismatch loss. One particular consequence of negligible geometrical effect is that one can use a relatively small representative part of a large module to characterize its integral non-uniformity loss. This brings about the question of size dependent effects, which we have answered by varying N in our simulations. Shown in Fig. 3.11 scaling dependence $SD \propto N^{-\alpha}$ with $\alpha \approx 0.74$ for random V_{oc} and $\alpha \approx 0.64$ for random Jsc distributions, points at a nontrivial physics underlying our results (for example, one would expect $\alpha = 0.5$ for a superposition of mutually independent PV elements), which is yet to be understood. From

the practical standpoint, our result shows that submodules of several tens of elements are quite representative statistically.

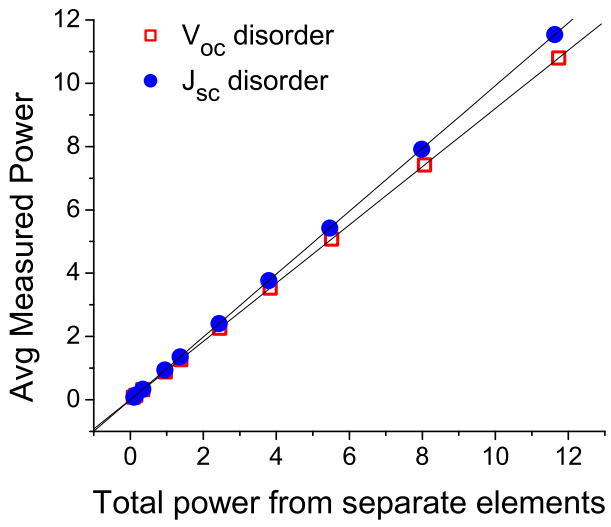

Figure 3.12: Size dependence of the module mismatch loss for the cases of randomly distributed V_{oc} and J_{sc} with the relative mean deviations of 13.2%.

The mismatch loss was estimated for modules of different size with the same statistical V_{oc} and J_{sc} distributions (Fig. 3.12). The results show that a certain fraction of power, independent of N and comparable to the relative fluctuations in random parameters, is lost due to the mismatch. While this has important practical consequences, the underlying physics remains to be explored.

Series and scribe resistances. Series and scribe resistances interfere with the nonuniformity effects. For a uniform module, it is well known that the series resistance lowers the efficiency. To the contrary, for a non-uniform module, lower value of R_s can enhance the efficiency loss.[16,24]. In turns, the latter effect depends on the scribe resistance (Fig. 3.13), which we explain by the role of shunting through scribe lines.

Conclusions Nonuniformity effects in large are PV modules exhibit several important features: 1) Geometrical distribution of nonuniformities across the module has only a minor effect on its efficiency; the latter is almost entirely determined by the distribution statistics (average and dispersion) as opposed to the geometry. 2) Module statistical characteristics exhibit non-trivial scaling dependencies vs. module size. 3) Mismatch loss is close to a certain fraction of module power and is independent of the module size. 4) Module series

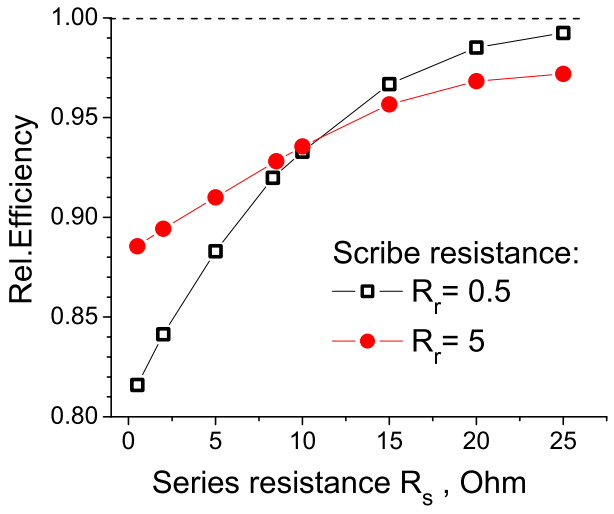

Figure 3.13: Relative efficiency vs. series resistance R_s for two different R_r's.

and scribe resistances interfere with nonuniformity effects offering a possibility to optimize combined nonuniformity and ohmic losses. 5) We have found the PSpice software to be an adequate tool for nonuniformity modeling.

3.4. Back contact and reach-through diode effects in thin-film photovoltaics

Introduction Applying a metal contact on a semiconductor device often results in a Schottky barrier which affects current collection. This is particularly detrimental to photovoltaics (PV) where the barrier acts as a diode in the "wrong" direction, opposite to the main junction, thus blocking the photo-generated charge carriers. This phenomenon, known as back barrier or back diode or back surface field, can affect all major PV materials, such as cadmium telluride (CdTe), silicon, and copper indium gallium selenide (CIGS).[4]

A common model for the back barrier effects is the equivalent circuit of a leaky back diode in series with the main junction photo-diode. One result of such modelling is a rollover in the first quadrant of the current-voltage (J-V) characteristics (Fig. 3.14 (b)); such a rollover has been observed many times.[4,25] Another obvious result is that, since the back diode does not generate photocurrent, it does not affect the device open circuit voltage (V_{oc}).

The latter prediction is however inconsistent with numerous observations that back contact recipes have profound effects on the device V_{oc}.[4] For example, there are several practically established recipes of making a "good" back contact for the case of CdTe based PV;[25–37]

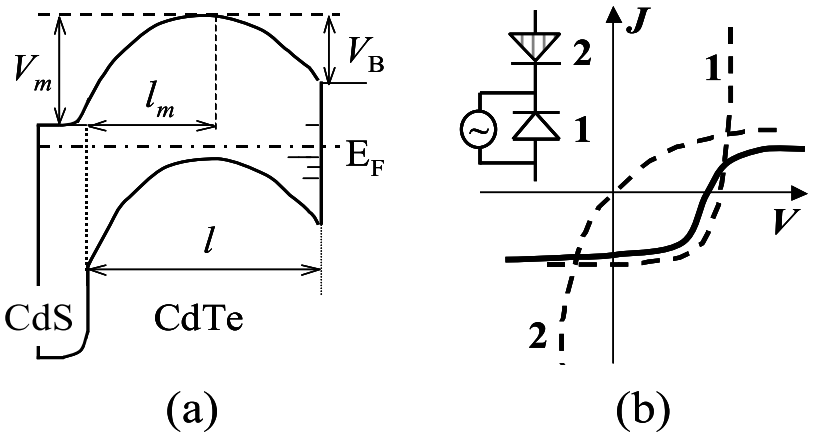

Figure 3.14: (a) Schematic band diagram of CdS/CdTe cell showing the main junction and back barriers in the absorber layer (CdTe); V_m and V_B are the main junction potential drop and the back barrier height, respectively, the dotted vertical line shows the metallurgical junction (b) J-V characteristics and equivalent circuit for a photovoltaic device with a back barrier operating in the back diode regime composed of the main junction J-V characteristic (1) and leaky back diode J-V characteristic (2).

other PV technologies have their own specific back contact recipes.

In this section we show that the back diode concept fails when the barrier grows above a certain height (in the range of practically significant values). Beyond the back diode regime, the system turns into a qualitatively new regime, which in the physics of semiconductor devices is known as the reach-through diode.[6] The transition between the back diode and reach-through diode regimes will be shown to depend strongly on the back surface state. This paves the way to understanding the back barrier effects on device performance. While our consideration and experimental results below mainly concerns thin-film CdS/CdTe devices, they lead to some general conclusions that may apply to other types of photovoltaics.

Back diode vs. reach-through diode regimes Shown in Fig. 3.14 is a band diagram of a PV device with a back barrier. For illustration purposes, its main junction is representative of a CdS/CdTe PV device. However, the specifics of the main junction do not have any significant effect on the discussion below, which focuses on the effects of the back contact on the device.

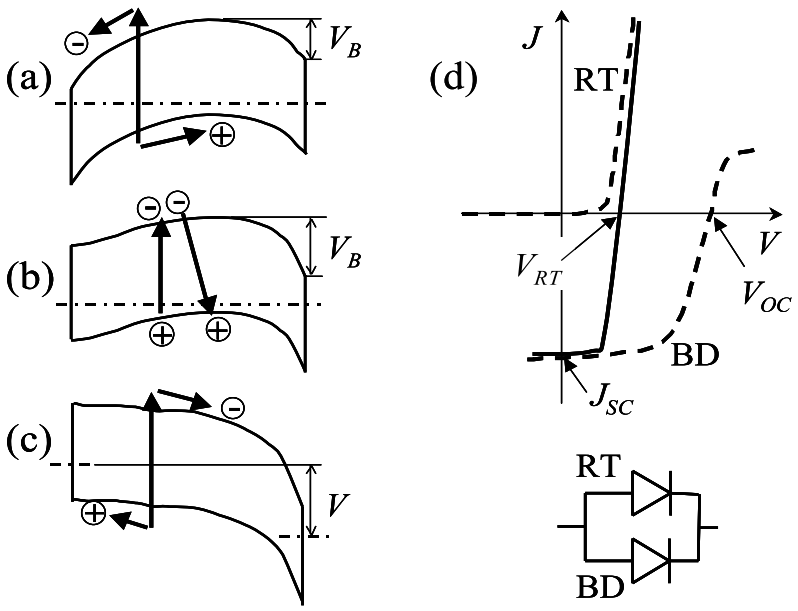

Figure 3.15: (a) Band diagram of the standard device absorber layer where the back contact is not very high and operates in the back diode regime. (b) Band diagram of a back barrier blocked absorber layer under short-circuit conditions. (c) Same under reach-through conditions, $V > V_{RT}$. (d) The corresponding J-V characteristic (RT) is shown in comparison with that of the standard device (with back barrier operating in the back diode regime (BD)). The solid line shows the J-V characteristics of a composite device consisting of the standard and reach-through devices in parallel. In the latter, the reach-through voltage (V_{RT}) appears to play the role of the open-circuit voltage when $V_{RT} < V_{oc}$.

We start by noting that the back diode concept implies no space charge accumulation, hence, the barrier is low enough to let a charge carrier (hole in the case of Fig. 3.15 (a)) leave the device before another carrier is generated nearby. When the back barrier height V_B grows above a certain value, it blocks the holes and the device supplies no current even under short-circuit conditions. Instead, the photo-generated electron hole pairs recombine as illustrated in Fig. 3.15 (b). Applying a forward bias above a threshold value $V > V_{RT}$, turns the device into the reach-through regime where the forward current is not blocked by the main junction barrier. It then flows freely provided that the window layer is transparent enough [Fig. 3.15 (c)], which we will assume in what follows. The corresponding J-V characteristics [Fig. 3.15 (d)] will have a threshold voltage V_{RT} which depends on the main

junction and back contact built-in potential (barrier) heights, V_m and V_B, respectively.

The latter dependence can be specified assuming uniform doping, which makes the electric potential parabolic in the coordinate. In particular, the parabolic potential maximum can be expressed in the terms of V_{m0} and V_B, where V_{m0} is the maximum potential V_m when no back barrier is present ($V_B = 0$). The reach-through condition requires that in response to the external bias V_{RT}, the position of the latter maximum shifts by l_m (Fig. 3.14 (a)) to approach the window layer edge. This enables one to estimate

$$V_{RT} = 2V_{m0}\left(1 - \sqrt{\frac{V_B}{V_{m0}}}\right) \tag{3.4}$$

Thus either a weak main junction (low V_{m0}, due to insufficient doping or other factors affecting the built-in voltage) or a strong back barrier (high V_B) will lead to low reach-through voltages V_{RT}.

The photo-generated charge carrier blockade can take place already for moderately high back barriers of several tenths of electronvolt, in the range of observed values,[25,29] as seen from the following estimate. The number of charge carriers overcoming the barrier by thermal activation per unit area per unit time is $\sim nv\exp(-V_B/kT)$, where v is the carrier velocity and n is the quasi-stationary electron concentration. This should become comparable to the recombination rate per unit area $l\gamma n^2$ to make the charge carrier blocking significant. Here γ ($\mathrm{cm^{-3}s^{-1}}$) is the recombination coefficient. We assume that recombination occurs uniformly over the film thickness l (Fig. 3.14) and the generation rate is high enough to result in quadratic recombination. The steady state balance implies the recombination rate comparable to the electron generation by the fully absorbed light of intensity I, in photons per time per area. Equating, in the order of magnitude, all of the above rates gives

$$V_B = \frac{kT}{2}\ln\left(\frac{v^2}{I\gamma l}\right). \tag{3.5}$$

For numerical estimate we use a one sun light intensity $I \sim 10^{17}$ $\mathrm{cm^{-2}s^{-1}}$ and velocity $v \sim 10^8$ cm $\mathrm{s^{-1}}$ corresponding to the anticipated kinetic energy of the order of $V_B \sim 1$ eV (note that such V_B is much greater than the thermal energy kT). Also, we assume a typical $\gamma \sim 10^{-10} - 10^{-12}$ $\mathrm{cm^3s^{-1}}$,[38] and $l \sim 1$ μm. This gives $V_B \sim 15kT \sim 0.4 - 0.5$ eV, which is in the range of practically significant values.

While oversimplified, the estimate in Eq. (3.5) can serve as a rough guide. For example, taking into account the effects of spacial separation of electrons and holes, and finiteness

of the light penetration length will change γ and I. Because these are logarithmically dependent, this change will not have too strong an effect on the above estimate in Eq. (3.5).

The most sensitive approximation behind Eq. (3.5) is that it completely neglects electron tunneling. The latter is more difficult to evaluate for it depends on the barrier shape, generally unknown. Also, such tunneling can be thermally and defect assisted, which makes it laterally nonuniform.[39–41]

Theoretical estimates of defect assisted tunneling (see review in Ref. 41) are based on the concept of rare yet most efficient N-defect pathways through the barrier. Electrons penetrate the barrier along these pathways in N successive tunneling steps of length $\approx L/N$ where L is the barrier width. Each step has exponentially large tunneling probability $\exp(-L/Na)$ compared to that without defects, $\exp(-L/a)$ where a is the electron wave function decay length. Because of the probability of N-defect pathways, statistical fluctuations in local defect concentration have an exponentially strong effect on tunneling. In particular, local spots with relatively low defect concentration are not suitable for tunneling and are described by the above estimate in Eq. (3.5). To the contrary, spots with relatively high defect concentration will provide efficient tunneling pathways. For them, the characteristic barrier height, above which the reach-through diode regime dominates, will obviously be higher than the estimate in Eq. (3.5).

The above theoretical consideration implies a generic band diagram (fig. 3.14 (a)), where a potential band offset at the CdS/CdTe interface does not form a potential barrier for the electrons. This simplification may be adequate for the case of CdS/CdTe devices[42]. In the alternative case of a significant potential barrier for holes between the window and absorber layer[43], the blocking effect will become even more significant.

We shall end this section with the conclusion that a device containing a back barrier can operate in either standard (back-diode) or reach-through diode regime. The latter takes place if the back barrier is high enough and has the J-V characteristics with zero short-circuit current (J_{sc}) and rather low "lift off" voltage V_{RT}, above which the current increases drastically [Fig. 3.15 (b)]. In particular, V_{RT} can be much lower than the standard device open-circuit voltage $V_{oc} \sim V_m$.

Reach-through microdiodes In photovoltaic devices, J-V characteristics with $J_{sc} = 0$ (illuminated) are of no interest. However, abnormally low "lift off" voltages (commonly re-

ferred to as a low V_{oc}) are a known phenomenon empirically attributed to the back contact.[36] In this subsection we show how the "low V_{oc}" feature can be explained by reach-through microdiodes, which are defined as local regions operating in the reach-through diode regime.

We also note that both the back barrier and the main junction are laterally nonuniform, as are interface barriers in many systems (see Refs. 16,44). In particular, while transparent enough on average, the back barrier can have rare microscopical "bad" spots of low hole transparency.[45] They and/or locally weak main junction spots turn the corresponding local regions into reach-through microdiodes. The latter are connected in parallel with "standard" microdiodes whose V_{oc} are independent of the back barrier height (as explained above).

For $V_{oc} > V_{RT}$, such a circuit exhibits a J-V characteristic with short-circuit current J_{sc} close to that of the standard microdiodes. This "standard" J_{sc} however combines with the apparent "low V_{oc}" whose role is played by the reach-through diode V_{RT} as illustrated in Fig. 3.15 (d). Such a J-V characteristic reproduces the observed "low V_{oc}" feature and explains how an optically inactive back surface can affect the device V_{oc}.

At first glance, it is counterintuitive that local spots of low back barrier transparency significantly decreases the system V_{oc}, for the current should flow around such spots, making their presence immaterial. However, exactly because of the photocurrent flowing around, such spots find themselves under significant forward bias where they become nonlinear shunts (illustrated in Fig. 3.16) and decrease the system V_{oc}.

Shunting by reach-through micro-diodes is similar to that by weak diodes analyzed in Ref. 16. We recall that the weak diode concept phenomenologically introduces micro-diodes with low V_{oc} and standard J_{sc}. It is immediately apparent from Fig. 3.16 that the diode shunting ability is due to its J-V characteristics in the first quadrant, and the value of J_{sc} is irrelevant. (In particular, Fig. 3.16 represents the same physics as Fig. 4 in Ref. 16). In view of this similarity, several important results of the weak diode theory can be extended to the case under consideration (given below in the terms and notations of this work).

(a) The effect of a reach-through micro-diode spans the screening length

$$L = \sqrt{(V_{oc} - V_{RT})/\rho J_{sc}}, \tag{3.6}$$

where J_{sc} is understood as a specific current (per area or length depending on the system dimensionality). The physical meaning of L is that the fluctuation in electric potential is balanced by the potential drop $J_{sc}L^2\rho$ across the resistive electrode of linear dimension L.

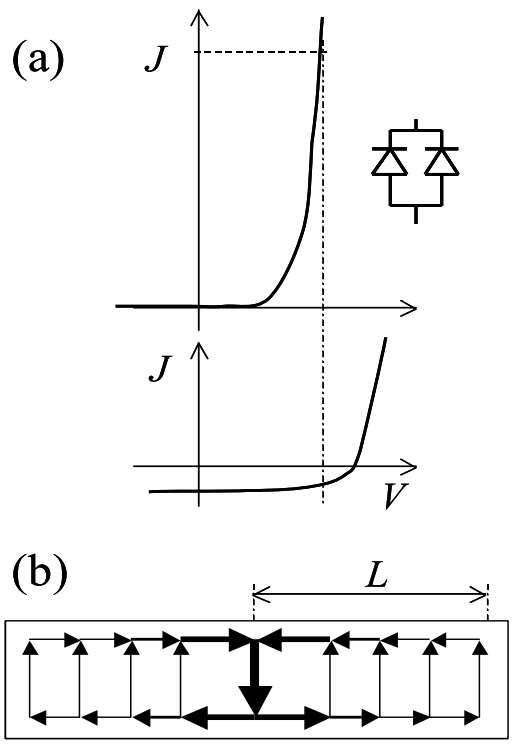

Figure 3.16: (a) Equivalent two-diode circuit (inset) and J-V characteristics of the reach-through micro-diode (shunting the current) and its more robust neighborhood (supplying the current). The reach-through micro-diode finds itself under forward bias and runs exponentially high forward current. (b) Current distribution in a system of robust diodes surrounding a reach-through diode. Fat arrow shows shunting current through the reach-through micro-diode, with polarity opposite to that of the photo-generated currents supplied by the majority of micro-diodes. L is the screening length.

It applies to both the one-dimensional (D=1) and two-dimensional (D=2) cell. For D=1, $L\rho$ and $J_{sc}L$ represent the resistance and current, and ρ is understood as the resistance per unit length. For D=2, the resistance is represented by the sheet resistance ρ and the current is $J_{sc}L^2$. The maximum screening length $L_{\max}$ corresponds to $V_{RT} = 0$ (dead shunt). It can also be shown that the minimum screening length L_{min} is defined by Eq. (3.6) with $V_{oc} - V_{RT} = kT/e$. The length L varies over a wide range depending on the sheet resistance and photocurrent, typically from 1 mm to 1 m.

(b) There is a dimensionless parameter

$$\xi \equiv \frac{1}{c}\left(\frac{b}{L_{min}}\right)^{D} \exp\left[\frac{2e(\overline{V}_{oc} - V_{RT})}{kT}\right], \tag{3.7}$$

such that when ξ grows through its critical value (of the order of one)[16,46] then the system undergoes a phase transition from the regime of small fluctuations to that of large fluctuations. Here c ($\ll 1$) is the dimensionless concentration of reach-through micro-diodes, b is a micro-diode linear size, and the macroscopically averaged open-circuit voltage is defined by

$$\overline{V}_{oc} = V_{RT} - \frac{kT}{e}\ln\left\{c + \exp\left[\frac{e(V_{RT} - V_{oc})}{kT}\right]\right\}. \tag{3.8}$$

(c) In the small fluctuation regime, the macroscopic open-circuit voltage only slightly fluctuates between nominally identical cells and is close to $\overline{V}_{oc}$. In the strong fluctuation regime, the measured V_{oc} is lower than $\overline{V}_{oc}$ and varies considerably between nominally identical devices.

We emphasize that the above mechanism of low observed V_{oc} implies robust micro-diodes with $V_{oc} > V_{RT}$ in parallel with reach-through microdiodes. In the opposite case of $V_{oc} < V_{RT}$, the presence of reach-through micro-diodes will have almost no effect on the device J-V characteristics [which can be understood from a diagram similar to Fig. 3.15 (d), but with $V_{oc} < V_{RT}$]. In other words, reach-through diodes are detrimental to strong main junction devices (high V_{SPV}, Table 3.3), while they should not affect weak main junction (low V_{SPV}, Table 3.3) cells (poorly doped, etc.).

Model predictions Summarized in Table 3.4 are predicted features related to the presence of local spots of low barrier transparency and corresponding reach-through micro-diodes. Here we briefly comment on each of the features; their experimental verification is described below.

Based on the above understanding of the "low V_{oc}" feature attributed to V_{RT} [Eqs. (3.4), (3.8)], and taking into account that V_{RT} does not depend on the light intensity I, the observed low V_{oc} is also predicted to be independent of I. This distinguishes the reach-through related low V_{oc} from other low V_{oc} causes, such as *e. g.* a weak main junction. (We recall that the latter leads to a readily verifiable $V_{oc} = const + \ln I$.)

The next feature seen from Fig. 3.4 is that since the back barrier is not functioning as a back diode in the reach-through regime, there will be no rollover in the J-V characteristics,

which appear abnormally steep, again quite different from the case of "good" high V_{oc} devices.

Based on the existing reach-through diode theory,[6,47] one can expect the J-V curve linearization related to the space-charge-limited current at high voltages, $J \propto v_s V$, where v_s is a saturated high field charge carrier velocity. v_s can depend on the light intensity; in the simplest approximation, $v_s \propto I$. The corresponding characteristics will be $J \propto VI$.

When low in concentration ($c \ll 1$), the reach-through micro-diodes do not affect the device surface photovoltage V_{SPV}. Indeed, since V_{SPV} is measured without back contact metal, different microdiodes are electrically insulated. Hence, the contribution from reach-through micro-diodes is small in the measure of $c \ll 1$. Therefore, removing the back metal from a low V_{oc} device will leave a surface with high $V_{SPV} > V_{oc}$.

The above-mentioned possibility of strong fluctuation regime leads to the prediction of possible extremely high variability between nominally identical devices with low V_{oc}. [Note however that the observed V_{oc} can be consistently low between nominally identical devices if $\xi \ll 1$ in Eq. (3.7).]

Finally, we recall that the case of $V_{RT} > V_{oc}$ makes the reach-through micro-diodes immaterial. This translates into the prediction that devices with low V_{SPV} (weak main junction) will not exhibit the above listed features.

Experimental verification In the experimental part of this work, we used a 0.12 μm thick n-type CdS and 3.5 μm thick p-type CdTe deposited by close-space sublimation (see Ref. 3). A transparent conductive oxide (TCO) layer of sheet resistance 12 $\Omega/\Box$ on a glass substrate (Tec15 glass from Pilkington) underlying the CdS was used as a front electrode. The structures underwent the standard anneal in the presence of $CdCl_2$ vapors known to improve electrical characteristics.[7] We prepared several types of devices implementing different combinations of main junction and back barrier parameters as described below.

Back contact deposition. In this work, different back contacts were used (see Table 3.3). Au and Cu/Au back contacts were deposited by evaporation on a cold substrate. ZnTe:N was deposited by reactive R.F. sputtering using 3% N_2 in the sputtering gas (Ar). The substrate temperature was kept at 360 °C. Ni was deposited by D.C. sputtering on a cold substrate.

Buffer layer technology. In several cases, the main junction was affected through the CdS interface where we additionally deposited (on the TCO) a 0.1 μm thick tin-oxide based buffer layer[8,9]. Its sheet resistance ($\approx 1.2 \cdot 10^4 \Omega/\Box$) was much higher than that of TCO, yet low enough to consider it a metal in the sense that its Fermi level lies above that of the CdS film. A buffer layer improves the main junction quality,[48–50] which shows up in significant V_{SPV} increase. In this study, samples with buffer layer were used as strong main junction devices. The strong junction was combined with "bad" back contacts (no-anneal Cu or ZnTe:N recipes; Table 3.3) or "good" back contact (Au in Table 3.3).

Table 3.3: Experimental verification of main junction vs. back contact quality predictions

Back Contact	TCO/CdS/CdTe Weak junction $V_{SPV} \simeq 550$ mV	TCO/buffer/CdS/CdTe Strong junction $V_{SPV} \simeq 800$ mV
Au Good BC	Voc = 540 mV	Voc = 815 mV
Cu/Au Bad BC	Voc = 490 mV	Voc = 650 mV
ZnTe:N/Ni Bad BC	Voc = 540 mV	Voc = 670 mV

Gold back contact. Based on its high work function,[6] Au is expected to form a good back contact with CdTe, which was experimentally verified.[25] We emphasize that unlike many conventional recipes, Au deposition was not followed by any anneal. In combination with a strong (buffer layer induced) junction, this led to a device efficiency up to 13%.

Conventional back contact. It is typical for CdS/CdTe solar cells that the back contact deposition is followed by an anneal step, called post-metal heat treatment. When Cu is used, the anneal triggers Cu diffusion, which improves both the main junction and the back barrier hole transparency.[10,11,51] For the case of ZnTe:N, the anneal lowers the film resistivity and the back barrier height.[52]

As opposed to the conventional approach, no anneal was performed after the back contact deposition in this work. Therefore, the back barrier height is rather determined by the difference in work functions between the metal and CdTe. As both Cu and ZnTe have similar

but lower work functions than Au,[6,53] the back barrier height V_B will be high, resulting in "bad" back contacts.

As illustrated in Table 3.3, devices without a buffer layer were all weak main junction cells showing $V_{SPV} \approx V_{oc}$. For the buffer layer devices only "good" Au back contact had $V_{SPV} \approx V_{oc}$; for all other back contact recipes the measured V_{SPV} ranged from 800 to 820 mV, much higher than their respective V_{oc}. Note that a no-anneal schedule used led to a poor quality back contact for all the recipes except pure Au.

In the mean time, the "no-buffer, no-anneal" samples in Table 3.3 showed relatively low $V_{SPV} \approx V_{oc}$ with clear evidence of J-V rollover. This is consistent with the model predictions for the case of $V_{RT} > V_{oc}$.

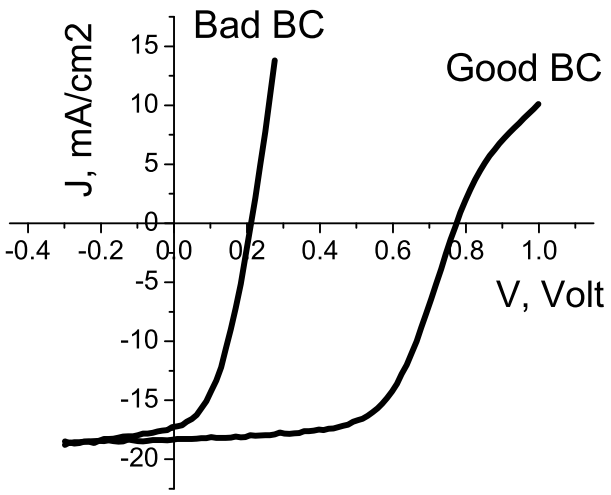

Figure 3.17: "Bad back contact" J-V characteristics for a cell without interfacial layer (IFL) and similar cell with good back contact obtained by application of the IFL (designed in Ref. 37) prior the cell metallization.

Shown in Fig. 3.17 are typical J-V characteristics that demonstrate how a back contact treatment can change the device V_{oc} and efficiency. It also shows that the low V_{oc} device has much steeper J-V curve, as opposed to the rollover in the "good" V_{oc} device, consistent with the predictions in the preceding section. In several cases of "low V_{oc}" devices, strong variability between cells in the same substrate was observed (measured V_{oc} varying, say, between 0.15 and 0.7 V). However, in other "low V_{oc}" cases, the measured low V_{oc} were rather consistent; it was in all cases consistent for the "high V_{oc}" devices. This can be attributed to the regimes of strong and weak fluctuations respectively, as described above.

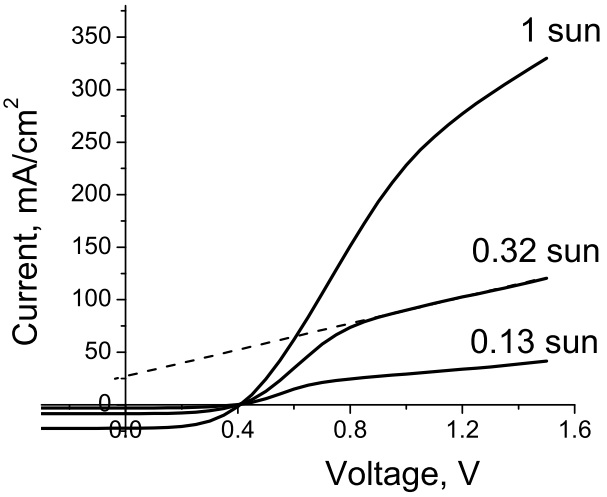

Figure 3.18: "Bad back contact" J-V characteristics for a cell without interfacial layer (IFL) for different light intensities indicated in the figure. Note V_{oc} independent of light intensities and extremely large forward currents. Dashed line shows linear dependence in the space-charge-limited current region.

The J-V characteristics for a "bad back contact" in Fig. 3.18 confirm the predicted reach-through diode features of low V_{oc} independent of light intensity, and steep J-V region that changes into a more gradual region $J \propto V$. The ratios of the photocurrents measured under different light intensities I turn out to be approximately the same in the short-circuit ($V < 0$) and space-charge limited regions ($V > 1$V) regimes (Fig. 3.19). Since it is known for the former regime that $J_{sc} \propto I$, we conclude that the relationship $J \propto I$ holds for the latter regime as well. Following reach-trough diode model, this can be attributed to the light dependent charge carrier velocity.

In the intermediate region between the reverse current and space charge limited current regions, the currents do not show any systematic dependence on I, consistent with the reach-through transport mechanism. In particular, a seemingly singular behavior in fig. 3.19 takes place in the intermediate region at biases close to the apparent V_{oc}. However, the latter V_{oc} is not the true V_{oc} but rather V_{RT}, that plays the role of V_{oc} in the reach-through regime. The particular value of $V_{RT} \simeq 0.4$ V is specifics to the device whose J-V characteristics in fig. 3.18. Other devices will show different V_{RT}, as illustrated in fig. 3.17.

We conclude that our data confirm all the model predictions.

Reach-through micro-diodes can exist in the above-described system due to either local

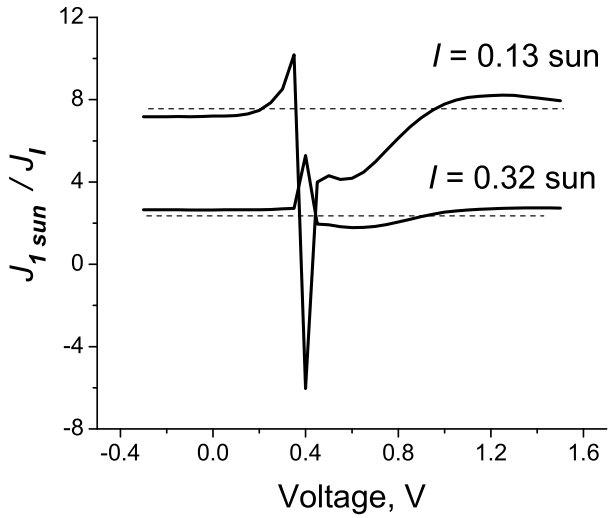

Figure 3.19: Ratios of the 1 sun to lower light intensity I currents versus voltage. The ratios are proportional to $1/I$ for the reverse current and space charge limited current regions.

spots of low barrier transparency or weak main junction. For example, pinholes in the absorber layer (missing CdS grains) can cause lower V_{RT}.

Practical consideration The present study suggests a novel approach to manufacturing CdTe/CdS devices. The main constituents of it are 1) buffer layer used to achieve high V_{oc} and 2) "cold" evaporated Au contact that does not require post metal heat treatment or special surface preparation. This enables one to consistently make $\sim 13\%$ devices with a relatively "thick" CdS layer (~ 1000 Å in our study).

We note that these devices do not have any intentional Cu, the latter considered one of the main degradation sources in CdTe photovoltaics.[54] Therefore, these devices are expected to exhibit superior long-term stability under light soak, preliminarily confirmed.

Conclusions In conclusion, we have presented an expanded analysis of the physics behind back contact effects in photovoltaics. A significant non-trivial finding is that rare local spots of low back barrier hole transparency or weak main junction can dramatically affect the device performance. Our understanding explains how changing the state of an optically inactive back surface affects the device open-circuit voltage and efficiency. This and several more specific predictions have been verified experimentally.

In addition, our work suggests a novel practical way of manufacturing Cu-free CdTe

Table 3.4: Reach-through microdiodes model predictions

PREDICTION	VERIFICATION
Low "Voc" independent of light intensity	yes (Fig. 3.18)
No rollover, steep J-V	yes (Fig. 3.17)
"Saturation" current depending on light intensity	yes (Fig. 3.19)
Removing the metal leaves surface with high V_{SPV}	yes (Ref. 36)
Anomalous variability between nominally identical very low V_{oc} devices	yes
No such phenomena for low V_{SPV} devices	yes

photovoltaics that could posses superior stability.

References

[1] Alvin D. Compaan et al., "The fabrication and physics of high efficiency CdTe thin film solar cells", annual technical report for the period Sep. 2001 to Aug. 2002, NREL contract No. NDJ-1-30630-02.

[2] Alvin D. Compaan et al., "The fabrication and physics of high efficiency CdTe thin film solar cells", annual technical report for the period Sep. 2002 to Aug. 2003, NREL contract No. NDJ-1-30630-02.

[3] C. S. Ferekides, D. Marinskiy, V. V. Viswanathan, B. Tetali, V. Palekis, P. Selvaraj, D. L. Morel, *Thin Solid Films*, **361-362**, 520 (2000).

[4] *Handbook of Photovoltaic Science and Engineering*, edited by A. Luque and S. Hegedus (Wiley & Sons, Chichester, UK 2003).

[5] M. Gloeckler, A. L. Fahrenbruch, and J. R. Sites, *Proceedings of the 3rd World Conference on Photovoltaic Energy Conversion*, Osaka, Japan, 11-18 May 2003, 2P-D3-52 (2003).

[6] S. M. Sze, *Physics of Semiconductor Devices* (Willey & Sons, New York, 1981).

[7] P. V. Meyers, C. H. Liu, and T. J. Frey, U.S. Patent No. 4,710,589 (1987).

[8] T. Takamoto, T. Agui, H. Kurita, M. Ohmori, Solar Energy Materials and Solar Cells, **49**, 219 (1997).

[9] J. M. Kestner, A. Chorney, J. J. Robbins, Y. Huang, T. L. Vincent, C. A. Wolden, and L. M. Woods, Materials Research Society Symposium Proceedings (2002), Vol. 730 (Materials for Energy Storage, Generation and Transport), p. 49.

[10] R. H. Bube, *Photovoltaic Materials* (Imperial College Press, London, 1998).

[11] S. E. Asher, F. S. Hasoon, T. A. Gessert, M. R. Young, P. Sheldon, J. Hiltner, and J. Sites, *Proc. 28th IEEE Photovoltaic Specialists Conference*, Alaska, 479 (2000).

[12] P. J. Sebastian and M. Ocampo, *J. Appl. Phys.*, **77**, 4548 (1995).

[13] G. Agostinelli, D.L. Botzner and M. Burgelman, Proceedings 29th IEEE Photovoltaic Specialists Conference, New Orleans, LA, 1822 May 2002 IEEE, New York, 2002, p. 744.

[14] I. Visoly-Fisher, S. R. Cohen, D. Cahen, and C. S. Ferekides *Appl. Phys. Lett.*, **83**, 4924 (2003).

[15] V.G. Karpov, A.D. Compaan and D. Shvydka, *Appl. Phys. Lett.* **80**, 4256 (2002).

[16] V.G. Karpov, A.D. Compaan and D. Shvydka, *Phys. Rev. B* **69**, 045325-1-12 (2004).

[17] Harin S. Ullal, Kenneth Zweibel, and Bolko G. von Roedern, 28^{th} *IEEE Photovoltaic Specialists Conference Proc.*, 418 (2000).

[18] D. Cunningham, K. Davies, L. Grammond, et al., 28^{th} *IEEE Photovoltaic Specialists Conference Proc.*, 13 (2000).

[19] M. Powalla, B. Dimmler, *Solar Energy Materials & Solar Cells* **75**, 27 (2003).

[20] L. Castaner and S. Silvestre *Modelling Photovoltaic Systems using PSpice* (Wiley & Sons, Chichester, UK 2002).

[21] L.L. Bucciarelli, Jr., *Solar Energy* **23**, 277 (1979).

[22] C. Gonzalez and R. Weaver, 14^{th} *IEEE Photovoltaic Specialists Conference Proc.*, 528 (1980).

[23] Ross

[24] U. Rau, P. Grabitz, and J. H. Werner, Appl. Phys. Lett., (2004) to be published

[25] A. Niemegeers and M. Burgelman, J. Appl. Phys. **81**, 2881 (1997).

[26] K. D. Dobson, O. Rotlevi, D. Rose, and G. Hodes, J. Electrochem. Soc. **149** G147 (2002).

[27] K. D. Dobson, I. Visoly-Fisher, G. Hodes, and D. Cahen, Adv. Mater. **2001**, 1495 (2001).

[28] D. Kraft, A. Thissen, J. Broetz, S. Fledge, M. Campo, A. Klein, and W. Jaegerman, J. Appl. Phys. **94**, 3589 (2003).

[29] D. W. Niles, X. Li, and P. Sheldon, J. Appl. Phys. **77**, 4489 (1995).

[30] D. Rioux, D. W. Niles, H. Hochst, J. Appl. Phys. **73**, 8381 (1993).

[31] X. Li, D. W. Niles, F. S. Hasoon, R. J. Matson, and P. Sheldon, J. Vac. Sci. Tech. A **17**, 805 (1999).

[32] V. P. Singh, O. M. Erickson, and J. H. Chao, J. Appl. Phys. **78**, 4538 (1995).

[33] B. Ghosh, R. W. Miles, M. J. Carter, and R. Hill, Electronics Letters, **29**, 438 (1993).

[34] R. W. Miles, B. Ghosh, S. Duke, J. R. Bates, M. J. Carter, P. K. Datta, and R. Hill, J. Cryst. Growth **161**, 148 (1996).

[35] F.F. Wang, A. L. Fahrenbruch, and R. H. Bube, J. Appl. Phys. **65**, 3552 (1989).

[36] D. Rose, R. Powell, U. Jayamaha, and M. Maltby, *Proceedings of the 29th IEEE Photovoltaics Specialists Conference, New Orleans, LA, 18-22 May 2002* (IEEE, New York, 2002), p. 555.

[37] Y. Roussillon, D. Giolando, Diana Shvydka, A. D. Compaan, and V. G. Karpov, Appl. Phys. Lett. **84**, 616 (2004).

[38] V. N. Abakumov, V.I. Perel, I.N. Yassievich, *Nonradiative Recombination in Semiconductors*, North-Holland (1991).

[39] P. Sutter, E. Sutter, and T. R. Ohno, Appl. Phys. Lett. **84**, 2100 (2004).

[40] D. Stievenard, X. Letartre, M. Lannoo, S. Ababou, G. Guillot, Phys. Rev., **B49**, 10354 (1994).

[41] M. E. Raikh and I. M. Ruzin, in *Mesoscopic Phenomena in Solids*, (eds Altshuller, B. L., Lee, P. A. and Webb, R. A.) 315 (Elsevier, 1991).

[42] J. Fritsche,D. Kraft, A. Thißen, T. Mayer, A. Klein, and W. Jaegermann Thin Solid Films **403-404**, 252 (2002).

[43] G. Agostinelli, D.L. Bätzner, and M. Burgelman Thin Solid Films **431-432**, 407 (2003).

[44] R. T. Tung, Appl. Phys. Lett. **58**, 2821 (1992).

[45] C. R. Corwine, A. O. Pudov, M. Gloeckler, S. H. Demtsu, J. R. Sites, Solar Energy Materials and Solar Cells **82**, 481 (2004).

[46] V. G. Karpov, Phys. Rev. Lett., **91**, 226806 (2003).

[47] J. L. Chu, G. Persky, and S. M. Sze, J. Appl. Phys. **43**, 3510 (1972).

[48] Bolko von Roedern, in *II-VI Compound Semiconductor Photovoltaic Materials*, edited by R.

Noufi, R.W. Birkmire, D. Lincot, and H.W. Schock, MRS Symposia Proceedings No. 668, Materials Research Society, Pittsburgh, (2001), p. H6.9.1.

[49] Bolko von Roedern, Physics of Photovoltaic Materials, Encyclopedia of Energy, Vol. 5, p. 47, Elsevier (2004).

[50] Y. Roussillon, D. Giolando, V. G. Karpov, Diana Shvydka, and A. D. Compaan, Appl. Phys. Lett. to be published.

[51] A.O. Pudov, M. Gloeckler, S.H. Demtsu, and J.R. Sites, K.L.Barth, R.A. Enzenroth, and W.S. Sampath, *Proceedings of the 29th IEEE Photovoltaics Specialists Conference, New Orleans, LA, 18-22 May 2002* (IEEE, New York, 2002), p. 760.

[52] J. Drayton, A. Gupta, K. Makhratchev, K. J. Price, R. G. Bohn, and A. D. Compaan, in *II-VI Compound Semiconductor Photovoltaic Materials*, edited by R. Noufi, R.W. Birkmire, D. Lincot, and H.W. Schock, MRS Symposia Proceedings No. 668, Materials Research Society, Pittsburgh, (2001), p. H5.9.1.

[53] F. El Akkad, A. Felimban, and F. Sallam, J. Vac. Sci. Technol. A **5**, 111 (1987).

[54] D. Grecu and A. D. Compaan, Appl. Phys. Lett. **75**, 361 (1999).

4. CHARACTERIZATION OF MATERIALS AND DEVICES

4.1. Overview

During the contract period we have developed several experimental techniques for in-depth photovoltaic device characterization. In our previous annual reports,[1,2] we described admittance spectroscopy for defect characterization, as well as low-light diagnostic method for nonuniformity detection. Strong emphasis continued to be placed on materials and cell characterization through the use of photoluminescence (PL) in different aspects such as nonuniformity diagnostics via PL mapping, study of laser-induced material degradation (PL fatigue),[1,2] and defect identification studies studies in finished devices (in collaboration with First Solar, LLC),[2] as well as in ion-implanted CdTe crystals (see Section 4.1). The latter effort has been extensively supported by our X-ray absorption fine structure (XAFS) analysis, described in Section 4.3 below.

4.2. Photoluminescence studies on ion-implanted CdTe crystals

Photoluminescence and electroluminescence are convenient and powerful methods to probe the material properties of an operating solar cell and to investigate the defect states in the active semiconductor material. PL and EL are particularly convenient for studies of the junction region. However, the unambiguous identification of the transitions responsible for the light emission, particularly in polycrystalline thin films has been elusive. Partly to address this difficulty of identification, we have made a series of measurements on single crystals which have received calibrated doses of known atoms from ion implantation. The disadvantage of ion implantation is that large numbers of defects are created, typically 1000 displacements for each atom implanted. In the academic year of 2001, we studied Te-implanted crystalline CdTe supplied by Keystone Crystal Co. PL studies on these implanted crystals showed that among the successive 30-minute anneals at temperatures from 350^{o}C to 425^{o}C in N_2 atmosphere, using a CdTe film as a proximity cap, 400^{o}C annealing allowed the implantation-induced damage to be removed.

The ion-implant-doped studies continued during the academic year of 2002. A study of Cu implants was accomplished. The ion implantation is done through collaboration with the atomic physics group at the University of Toledo with the accelerator in the Physics

and Astronomy Department. The positive Cu ions were implanted into crystalline CdTe at 3 different energies: 440, 220 and 100 keV in the ratio of 78%, 14% and 8% to obtain total doses of $2.8\text{x}10^{11}$, $2.8\text{x}10^{12}$ and $2.8\text{x}10^{13}/\text{cm}^2$. The projected range and range straggling are respectively 0.1784 and 0.099 μm from Monte Carlo calculations using "SRIM" - The Stopping and Range of Ions in Matter).[3] These energies produce project range matching the absorption length of 0.09 μm for the 488nm Ar laser and 0.35 μm for the 752nm Kr laser used for PL excitation. Annealing at 400^{o}C in N_2 was done to remove most of the vacancies and interstitials produced by the implanted ions.

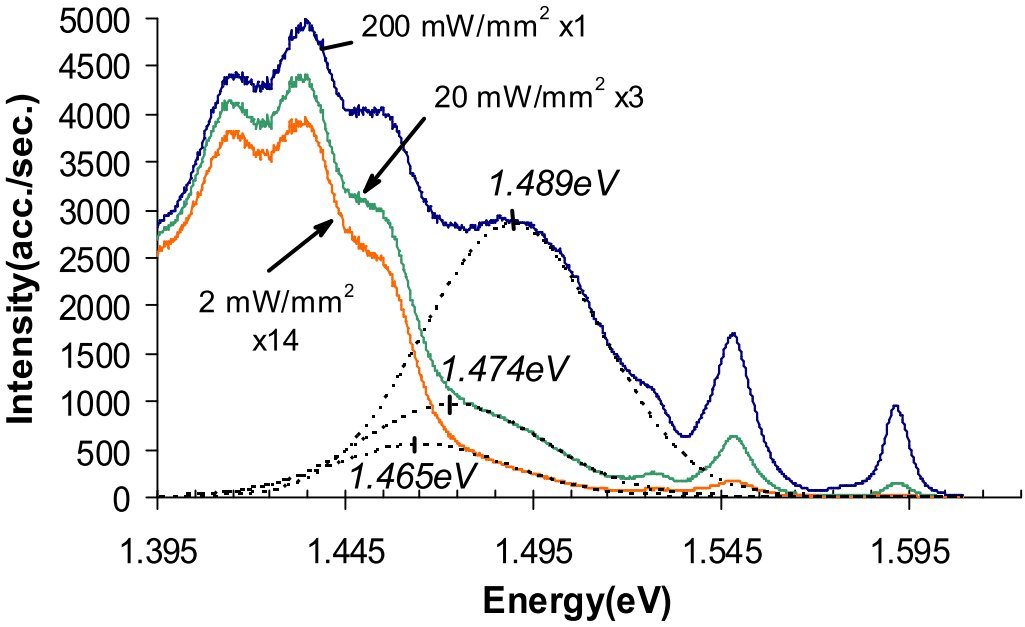

Figure 4.20: Power-dependent photoluminescence on $2\text{x}10^{13}/\text{cm}^2$ Cu-implanted and annealed sample excited by 488 nm Ar laser. Broad peak at 1.47 eV shifts to higher energy with laser power. Dashed lines: peak of DAP transition obtained from deconvolution (centers of peaks are labeled); solid lines: data.

Low temperature (10K) PL from the implanted and annealed crystal CdTe was studied

at excitation power densities of approximately 2, 20 and 200 mW/mm^2 ($\sim$2, 20, and 200 suns) to help identify the origin of the various features. For example, the bound-exciton peak near 1.593 increases superlinearly with laser intensity whereas the deep donor-acceptor pair transitions near 1.44 eV are sublinear in excitation intensity. The Cu-implanted crystals have a new peak at 1.46-1.49 eV which shows a characteristic shift toward higher photon energies with increasing excitation intensity. This helps to identify this peak as arising from the spatial distribution of donor-acceptor pairs. We suggest that this peak arises from a Cu acceptor substitutional on a Cd site together with an as yet unknown donor.

This effort on ion-implanted CdTe crystals and films was continued with the implantation of Cl ions in the academic year of 2003 and 2004 and was expanded through collaboration with Nikko Materials Co., Ltd (NM), who supplied high quality single crystal CdTe for our further PL study. The PL on their undoped wafer, figure 4.21 a), suggests extremely low defect concentrations. The normal broad defect band from 1.39 to 1.44 eV (see, for example figure 4.21 b)) is not observed on the Nikko wafer. The phonon-assisted exciton (1.577eV) and bound exciton (1.588-1.592eV) emissions are much stronger than usually observed in wafers from Keystone Crystal Co. (KC). Although a second wafer from NM had defect emission similar to that of the KC wafer, it still had strong exciton emission, as shown in Figure 4.21 b).

Due to the small size of the higher quality CdTe wafer supplied by NM, we could only prepare one Cl-implanted piece of this type. A power-depent PL study was done on these Cl-implanted high quality CdTe wafers before and after annealing. The PL data (not shown) were obtained with five different laser excitation powers in the range from 1 to 125 mW/mm^2 for both 488nm and 752nm lasers. Deconvolution of spectra is in progress to obtain the intensity of each peak, such as free-exciton, bound-exciton, free-to-bound and donor-acceptor pair (DAP) transitions, so that the origin of these transitions can be identified.

A more extensive study of Cl implants was done on the second quality CdTe wafer from Nikko Materials Co. $Cl^{++}$and Cl^{+} ions were implanted into the crystal, at three different energies: 400, 200 and 100 keV with fractional doses in the ratio of 72.5%, 18.8% and 8.7% to obtain total four different doses of 1.22x10^{12}, 4.07x10^{12}, 4.07x10^{13} and 4.07x10^{14} /cm^2 (corresponding to Cl concentrations respectively 3x10^{16}, 1x10^{17}, 1x10^{18}, 1x10^{19} /cm^3). The projected range and range straggling at 400 keV are, respectively, 0.2642 and 0.1429 μm obtained from SRIM.[3] Thus we expect approximately uniform implanted ion concentrations

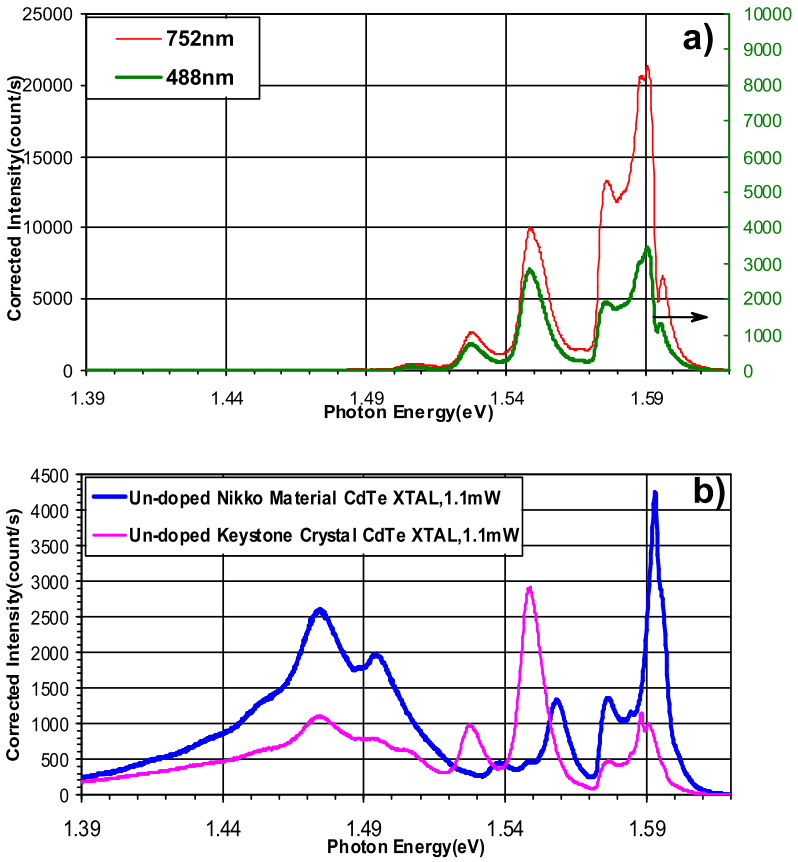

Figure 4.21: a)PL on undoped first quality CdTe wafer from Nikko Materials Co., Ltd with high quality, excited by 350 sun laser; b)PL on second quality CdTe wafer from Nikko Materials Co., Ltd and Keystone Crystal, excited by 100 sun 752nm lasers.

to a depth of $\sim$0.4 μm. These energies were chosen to match the absorption length of the 752 nm PL excitation laser (0.35μm). Annealing at 400^{o}C in N_2 for 30 minutes was done to remove most of the vacancies and interstitials produced by the implanted ions.

Photoluminescence was collected before and after annealing. The dramatic changes after annealing are presented in Figure 4.22. The intensities of the whole spectrum, including defect-band, band-to-band, and bound-exciton emission, increase with Cl dopant concentration. The broad band at 1.54 eV in the spectrum of the wafer with 1x10^{19} /cm^3 Cl, is suspected as being due to insufficient annealing. Longer times or higher temperatures may

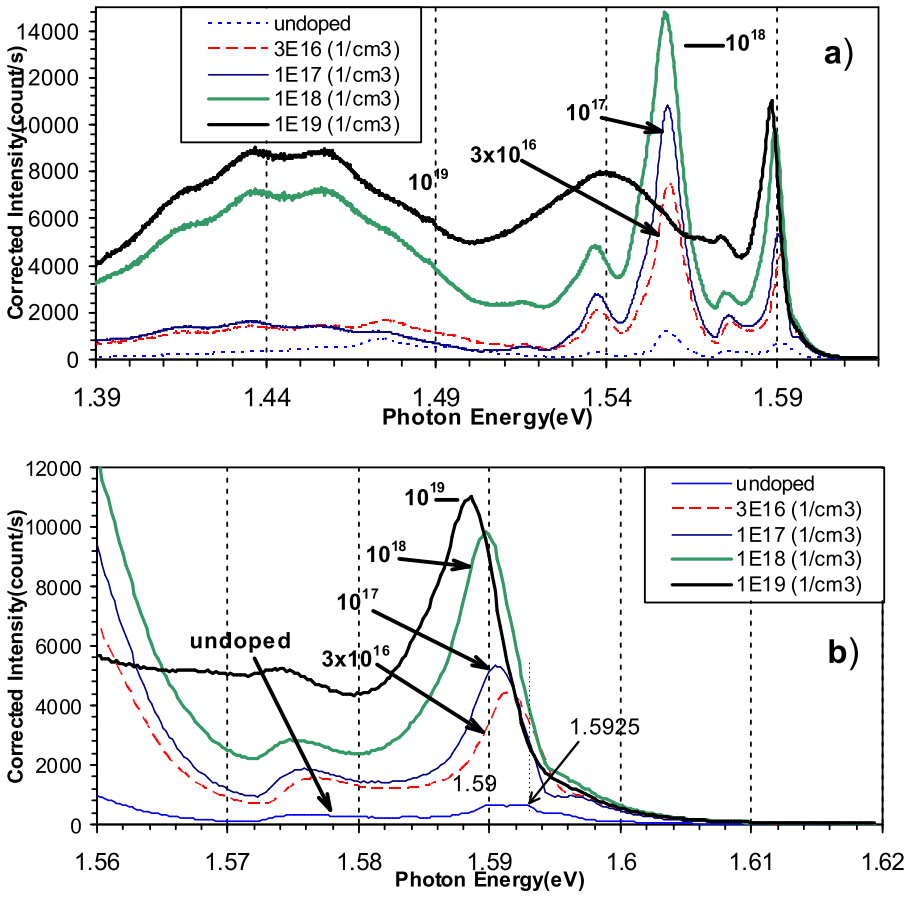

Figure 4.22: PL FROM annealed Cl-implanted CdTe wafer from Nikko Materials Co., Ltd , excited at 37 sun, 752nm. a) full spectrum; b) bound-exciton band shifting to lower energy as Cl dopant increases.

be necessary for crystal regrowth when the implanted region is fully amorphized as is likely the case here. The bound-exciton emission peak shifts to lower energy as the Cl concentration increases as the D^{o}X line at 1.590 eV starts to predominate and overwhelm the other suspected D^{o}X peak at 1.5925 eV(Figure 4.22b), both of which are distinguishable in the PL of the undoped sample. We suggest that the peak at 1.590 eV is the D^{o}X transition where the donor is Cl_{Te} with the electron binding energy E_d= 14 meV[4] and the CdTe band-gap

E_g= 1.604 eV at 10K. The other peak at 1.5925 eV appears also in the intrinsic CdTe crystal and there is no other implanted element besides Cl, we suggest this is an exciton bound to a non Cl-related donor.

4.3. Cu K-edge XAFS in CdTe before and after treatment with $CdCl_2$

X-ray absorption fine structure (XAFS) is a powerful technique for understanding the lattice environment around specific atoms.[5] We have used the fine structure in the Cu K-edge x-ray absorption spectrum to help elucidate the lattice location of Cu in polycrystalline, thin-film CdTe solar cells. In particular, we have studied how the typical $CdCl_2$ vapor treatment in dry air changes the local environment of the Cu in CdTe. Copper is found to bond to tellurium in form of Cu_2Te in the as-deposited CdTe film but mainly bond to oxygen as Cu_2O when Cu is diffused into films with prior vapor $CdCl_2$ treatment in air.

The 2-3 micron CdTe layers were magnetron sputtered at $\sim 250^oC$ onto fused silica substrates.[6] All the samples were prepared with 40 - 200Å evaporated Cu layers. Diffusion in N_2 at 150 or 200^oC for at least 45 minutes was applied to all samples. On some of the samples, short 5% hydrochloric acid etchings were also applied to remove any metallic copper left on the film surface. Some of the samples were annealed at 385^oC in $CdCl_2$ vapor in dry air for 30 minutes, before Cu deposition, diffusion and etching. These samples were compared to the non-chloride treated samples.

With assistance from Dr. Jeff Terry, data were obtained at the Materials Research Collaborative Access Team (MR-CAT) beamline at the Advanced Photon Source (Argonne IL) with the system shown in Fig. 4.23. The Cu K-edge x-ray absorption spectra of the Cu-doped CdTe samples were collected in a fluorescence geometry with a 13-element high purity Ge detector, by setting a 600 eV wide window at the position of Cu Ka (8048 eV) in the fluorescence spectrum, since the copper fluorescence intensity is proportional to the absorption by copper in the thin films. Reference powders of CuO, Cu_2O, $CuCl_2$ and Cu_2Te were applied to the adhesive of several layers of Kapton tapes and the absorption spectra were collected in the transmission geometry with detection by a N_2 ion chamber (Transmitted Intensity Monitor).

The X-ray absorption fine structure spectrum from the absorption edge of the element itself and a point usually 50 eV beyond the threshold is called XANES (X-ray Absorption

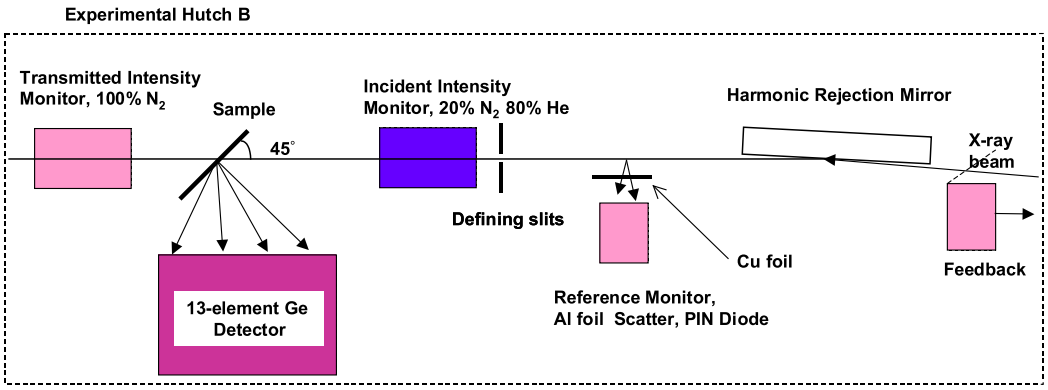

Figure 4.23: Experimental setup at MR-CAT.

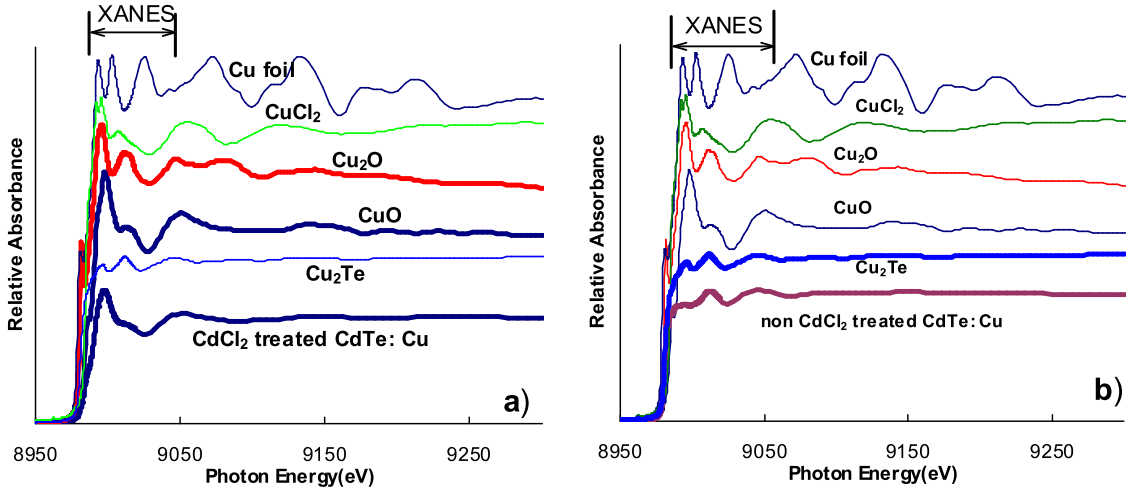

Figure 4.24: XAFS spectra emphasizing on the XANES region. a) Non-chloride treated CdTe films with diffused copper show features similar to Cu2Te; b) chloride-treated CdTe films with diffused copper show features similar to Cu2O and CuO.

Near Edge Structure). As shown in Fig. 4.24, comparison with reference materials in the XANES region usually helps to understand the predominant chemical bonds surrounding the core atoms in unknown samples. Before $CdCl_2$ treatment all of the CdTe films are observed to have features similar to Cu_2Te (see Fig 4.24a). However, the films with $CdCl_2$

treatment show features most similar to Cu_2O and CuO (see Fig. 4.24b). For convenience of comparison, absorption curves in relative magnitude are plotted in Fig. 4.24.

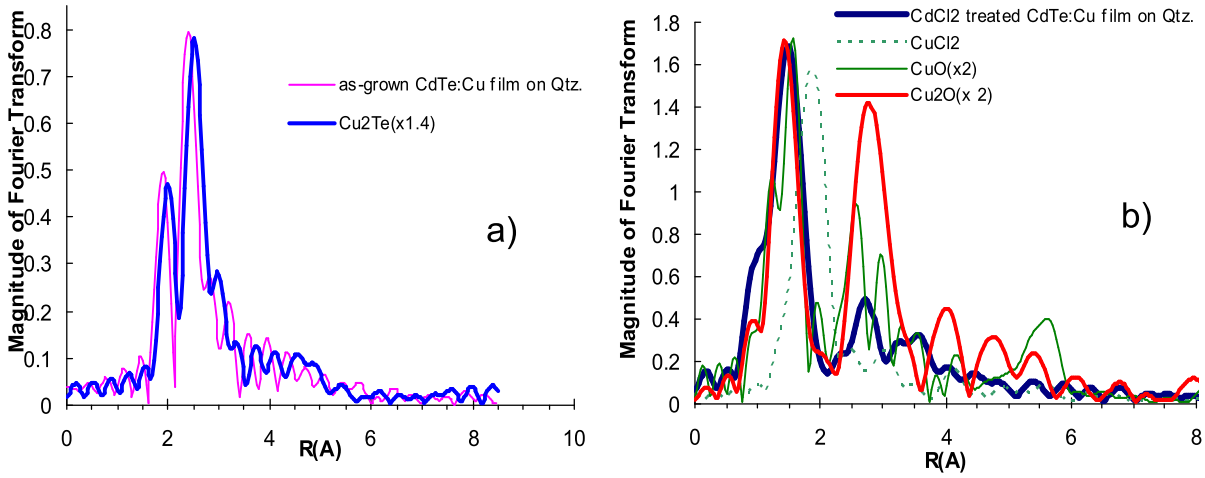

Figure 4.25: Fourier Transform of EXAFS.

EXAFS (Extended X-ray Absorption Fine Structure) refers to the periodic oscillatory structure in the absorption spectrum beyond the edge, is extracted from the x-ray absorption spectra by removing the background and is usually plotted in k (wave number) space. Finally the Fourier transform of this fine structure vs. r is computed.[5] Our analyses were performed through IFEFFIT an interactive program for XAFS analysis.[7]

The magnitudes of the Fourier transform (FT) for the two cases - without $CdCl_2$ treatment and with $CdCl_2$ - are shown in Fig. 4.25, although coordinates of peaks are not the real distance of neighbors from the core atoms, since photoelectrons are scattered by the outer electron shells of neighbor atoms instead of their nuclei. In the magnitude of the Fourier transform of Fig. 4.25a, we also observe that the strongest peak at 2.42 Å is shift to shorter distance from origin by about 0.1 Å than the one in cuprous telluride, but otherwise there is a strong correspondence.

For the films with $CdCl_2$ treatment and then doped with Cu, the shape of the FT of EXAFS and the position of the peaks are substantially different. Thus, we infer that the chemical environment of the typical copper atom is substantially changed from untreated

films doped with Cu and strongly depends on whether the CdTe films are Cl treated prior to Cu diffusion. The first peak resides at a position neither the same peak as cuprous telluride, Cu_2Te, nor cupric chloride, $CuCl_2$, but corresponds closely to cuprous oxide, Cu_2O at 1.50 Å, as shown in Fig. 4.25b. Since the second nearest neighbors of copper in cuprous oxide are copper atoms,[8] the fact that the second nearest neighbor peaks, in Fig. 4.25b, are very different suggests that we are not seeing nano-crystal inclusions of cuprous oxide but rather copper-oxygen clusters formed in the film or quite likely along the grain boundaries. The magnitude of the FT mostly depends on the coordination number in the neighbor shell. Further theoretical modeling shown below gives additional information on bond lengths and coordination numbers.

We also observed that the features similar to Cu_2O in $CdCl_2$ treated CdTe films are removable by HCl acid etching. After 10 seconds of etching in 9% HCl acid, most remaining copper atoms are found to be bound with Te as in the non-treated CdTe films, with a small portion of copper bound with O as Cu_2O.[9]

To avoid the complications of HCl etching on the $CdCl_2$ treated CdTe film, we prepared a sample using the same procedure as before but without etching and with a longer diffusion time. The 2.5 micron CdTe layers were magnetron sputtered at $\sim 250^oC$ onto fused silica substrates, followed with 40 Å evaporated Cu layers and diffusion in flowing N_2 at 200^oC as all other samples. The diffusion time for this sample, now even, was 4.5 hours rather than 30 minutes as other samples.

The Fourier transform of the EXAFS of this long-diffused, $CdCl_2$ treated CdTe:Cu film confirms that most copper is bound with oxygen as CuO in a treated CdTe film, as shown in Fig. 4.26(a). The major peak at 1.50Å refers to the 1st neighbor shell around copper atoms, which is only a small shift from the 1st neighbor shell of CuO reference at 1.56Å. However some of the copper in the film appears to bond with Te, as shown in Fig. 4.26a), the peak at 2.45Å and the shoulder at 2.0Å compared with the two peaks of Cu_2Te (refer to Fig. 4.25a)). This can be explained if most Cu_2O decomposed into CuO and Cu as a result of the 4.5 hours' heating in N_2, while the elemental copper atoms diffuse into the CdTe bulk and form Cu_2Te.

We also did an XAFS scan on CuCl to compare with $CuCl_2$. The Fourier transform of CuCl and $CuCl_2$, Fig. 4.26 b), shows similar bond length and structure except for weaker magnitude of scattering, which is reasonable for the smaller coordination number of copper

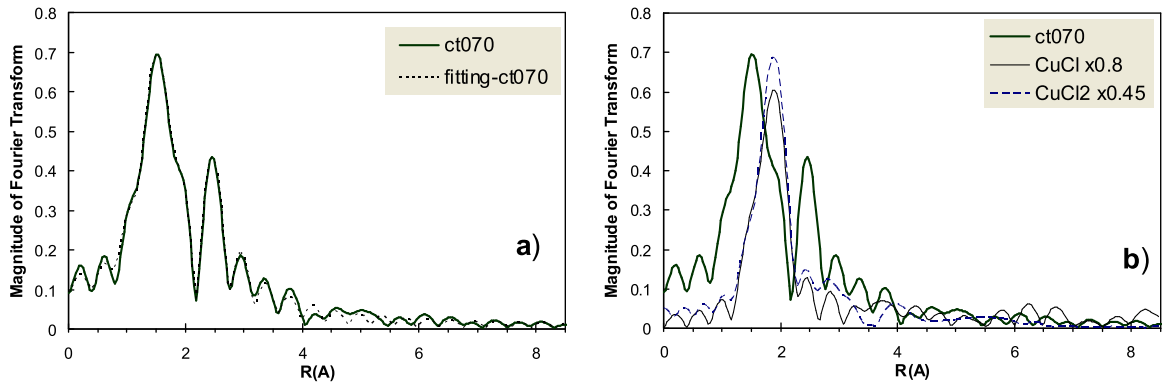

Figure 4.26: a) Fourier Transform of $CdCl_2$ treated CdTe:Cu with long diffusion (ct070) and theoretical fitting; b) comparison of CdTe:Cu (ct070) with CuCl and $CuCl_2$.

in CuCl. Although CuCl is more enthalpy of formation than $CuCl_2$, it is not proved to exist in $CdCl_2$ treated films by the XAFS experimental data. Neither CuCl nor $CuCl_2$ is found to have same bond as in Cl treated CdTe:Cu films.

In the last quarter of this contract, we used the computer modeling program FEFF to fit the EXAFS data and obtained detailed information about copper local structures in polycrystalline CdTe after different processing. FEFF is an automated program for ab initio multiple scattering calculations of XAFS and XANES spectra for clusters of atoms. The code yields scattering amplitudes and phases used in IFEFFIT, as well as various other properties. And then IFEFFIT combines the scattering amplitudes and phases of all the selected paths to simulate the real spectrum. Spectra of reference samples were fitted first to determine the most important contributing paths so that the paths that also contribute in unknown samples could be chosen. Overall threshold energy shift(ΔE_o), product ($N*S_o^2$) of coordination number(N) and overall amplitude parameter(S_o^2) of each path, mean square disorders(σ^2), and path lengths(R) were automatically computed in IFEFFIT as fitting parameters.

As shown before, films without prior $CdCl_2$ treatment are observed to have features similar to Cu_2Te. From the fitting (Fig. 4.27a), the first and second strong peaks in the

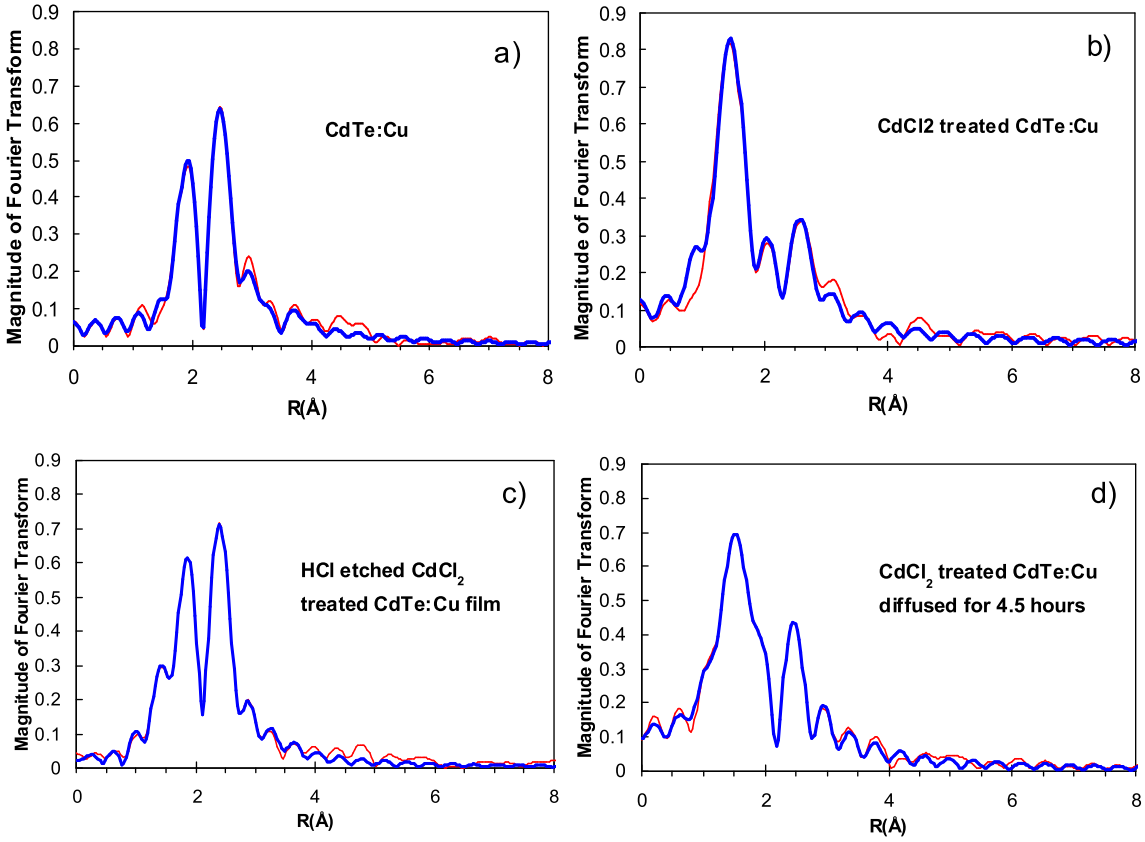

Figure 4.27: Fourier transform of Cu K-edge EXAFS function. Fine lines: experimental data, thick lines: theoretical fitting.

Fourier transforms indicate Te and Cu neighbors around Cu in as-deposited CdTe film (Table 4.5), forming clusters similar to Cu_2Te structure.[8] Meanwhile these Cu-Te and Cu-Cu bonds are observed in all the copper-diffused CdTe films despite the history of the films.

In the case of $CdCl_2$ treated CdTe films followed by copper diffusion(Fig. 4.27b), the predominant peak is identified as arising from oxygen neighbors around copper with coordination number of 1.4 at a distance 1.88 Å, which is only 0.03 Å farther than the nearest neighbor (oxygen) from copper atoms in a Cu_2O crystal.[8] Since besides this Cu-O bond no other bond same as in Cu_2O was found, it suggests Cu impurities do not form Cu_2O inclusions in chloride treated polycrystalline CdTe. Other two minor peaks are identified as Cu-Cu and Cu-Te bonds same as in as-deposited films and Cu_2Te except for 0.06 Å and

0.15 Å distortions respectively. Our first sample that was discovered with Cu_2O is actually protected by 55 Å Au from oxidization by air, which was deposited right after Cu evaporation. This convinced us that the Cu_2O in $CdCl_2$ treated CdTe polycrystalline film resides in the film (e.g., at grain boundaries as was proved later), instead of arising from metallic copper left on the film surface subsequently oxidized when exposed to air.

Cu in as-deposited CdTe film					Cu in $CdCl_2$ treated CdTe film				
bond scattering	N	R(Å)	σ^2(Å^2)	ΔE_o	bond scattering	N	R(Å)	σ^2(Å^2)	ΔE_o
					Cu-O(Cu_2O)*	1.4	1.88	0.0012	
Cu-Cu	2.6	2.27	0.0275	3.3	Cu-Cu	1.6	2.28	0.0130	4.9
Cu-Cu	1.4	2.51	0.0057		Cu-Cu	4.4	2.51	0.0175	
Cu-Te	3.5	2.56	0.0219		Cu-Te	4.6	2.52	0.0314	

Cu in $CdCl_2$ treated CdTe film followed by *HCl etching*					Cu in $CdCl_2$ treated CdTe film with *long diffusion*				
bond scattering	N	R(Å)	σ^2(Å^2)	ΔE_o	bond scattering	N	R(Å)	σ^2(Å^2)	ΔE_o
Cu-O(Cu_2O)*	0.8	1.92	0.0058		Cu-O(CuO)*	1.0	1.90	0.0057	
Cu-Cu	8.5	2.30	0.0289	2.7	Cu-Cu	1.2	2.32	0.0018	2.2
Cu-Cu	6.3	2.56	0.0167		Cu-Cu	9.5	2.57	0.0147	
Cu-Te	3.0	2.55	0.0095		Cu-Te	3.4	2.56	0.0062	

Table 4.5: FEFF fitting results on parameters of local structure around Cu atoms in different CdTe polycrystal films. Note: (1) $(Cu_2O)^*$, $(CuO)^*$ mean contribution from Cu-O bonds selected from Cu_2O or CuO crystal structure respectively; (2) All the other scattering paths arise from Cu-Cu and Cu-Te bonds selected from the Cu_2Te structure; (3) Since single scattering paths are the ones with strongest scattering magnitudes, we are presenting only single scattering paths obtained in the fitting and ignore other multiple scattering paths. For example, the path Cu-Te means an electron emitted from Cu atom is scattered back by the neighbor Te atom, and returns to the initial Cu atom.

Some of the chloride treated samples were chosen for etching by 9% HCl acid for 10 seconds, right before collecting EXAFS signal. The experimental and theoretical (Fig. 4.27

and table 4.5) fitting results suggest that most copper bond to Te and Cu by forming Cu_2Te clusters with only small portion of them bond to oxygen. This is consistent with the much faster etching rate of Cu_2O in HCl acid than Cu_2Te. Concerning less than 10 seconds HCl etching, we suggest this is evidence that Cu_2O formed in $CdCl_2$ treated films primarily locates along grain boundaries, where likely HCl could reach and dissolve the Cu_2O in such short period.

Theoretical fitting on the EXAFS of the sample with 4.5 hours diffusion (Fig. 4.27d and table 4.5) indicates the primary peak arising from oxygen neighbor from distance 1.9 Å with a coordination number of 1.0 as the structure in CuO. We do not observe the second primary peak arising from next nearest neighbor of copper atoms at distance 2.9 Å as in CuO,[8] which demonstrates no clusters of CuO formed in this heating stressed CdTe film.

Since chloride treatment is always performed before copper evaporation and diffusion, it suggests that this process prepares an oxidizing environment in CdTe films and when copper diffuses in, with higher electron affinity than Te, O could oxidize Cu and form Cu_2O on grain boundaries prior to Te. Cu_2O has interesting properties: it is cubic (a=4.27 Å), a p-type semiconducting oxide (in fact, one of the few such binary oxides), and a direct band gap semiconductor with E_g ~2.0 eV. Covering the boundaries of CdTe grains with another direct-band-gap semiconductor having E_g ~2.0 eV, Cu_2O probably plays a role in passivating grain boundaries. The band gap mismatch between Cu_2O and CdTe could inhibit grain boundary recombination. Similar effects have been observed in real CdTe solar cells by Iris Visoly-Fisher and David Cahen[10] using scanning probe microscopies.

References

[1] Alvin D. Compaan et al., "The fabrication and physics of high efficiency CdTe thin film solar cells", annual technical report for the period Sep. 2001 to Aug. 2002, NREL contract No. NDJ-1-30630-02.

[2] Alvin D. Compaan et al., "The fabrication and physics of high efficiency CdTe thin film solar cells", annual technical report for the period Sep. 2002 to Aug. 2003, NREL contract No. NDJ-1-30630-02.

[3] James Ziegler, SRIM, the Stopping and Range of Ions in Matter, http://www.srim.org/.

[4] D. M. Hofmann, P. Omling, and H. G. Grimmeiss, "Identification of the chlorine *A* center in CdTe", *Phys. Re. B*, **45**, 11, 6247-50 (1992).

[5] D. C. Koningsberger and R. Prins, *X-ray Absorption: Principles, Applications, Techniques of EXAFS, SEXAFS and XANES* (John Wiley & Sons, New York, 1988).

[6] M. Shao, A. Fischer, D. Grecu, U. Jayamaha, E. Bykov, G. Contreras-Puente, R.G. Bohn, and A.D. Compaan, "Radio-frequency-magnetron-sputtered CdS/CdTe solar cells on soda-lime glass," *Appl. Phys. Lett.* **69**, 3045-3047 (1996).

[7] Developed by Matte Newville, http://cars9.uchicago.edu/ifeffit/.

[8] Ralph W. G. Wayckoff, *Crystal Structures*, 2nd ed., V.1, 333-4 (1963).

[9] X. Liu, A.D. Compaan, Jeff Terry, "Cu K-edge EXAFS Study $CdCl_2$ Treatment Effect on CdTe Film", National CdTe R&D Team Meeting; Perrysburg, OH; February 26-27, 2004.

[10] Iris Visoly-Fisher, Sidney R. Cohen, and David Cahen, *Appl. Phys. Lett.* **82**, 556-8 (2003).

5. PUBLICATIONS

5.1. Refereed papers published or in press (9/1/01 - 8/31/04)

1. "All sputtered 14% CdS/CdTe thin-film solar cell with ZnO:Al transparent conducting oxide", Akhlesh Gupta and Alvin D. Compaan, Appl. Phys. Lett., **85**, 684 (2004).

2. "14% sputtered thin-film solar cells based on CdTe", A.D. Compaan, A. Gupta, J. Drayton, S-H Lee, S. Wang, Physica Status Solidi (b) **241**, 779 (2004).

3. "Back contact and reach-through diode effects in thin-film photovoltaics", Y. Roussillon, V. G. Karpov, Diana Shvydka, J. Drayton, and A. D. Compaan, J. Appl. Phys., to appear in December 1, 2004 issue.

4. "E^2 phase transition: thin film breakdown and Schottky barrier suppression", V. G. Karpov, Diana Shvydka and Y. Roussillon, Physical Review B, to appear in October 12, 2004 issue.

5. "Reach-through band bending in semiconductor thin films, Y. Roussillon, V. G. Karpov, Diana Shvydka, A. D. Compaan, and D. M. Giolando, Appl. Phys. Lett., to appear in October 4, 2004 issue.

6. "Random diode arrays and mesoscale physics of large-area semiconductor devices", V. G. Karpov, A. D. Compaan, and Diana Shvydka, Phys. Rev. B **69**, 045325-1-12 (2004).

7. "Lock-in thermography and nonuniformity modeling of thin-film CdTe solar cells", Diana Shvydka, J.P. Rakotoniaina, and O. Breitenstein, Appl. Phys. Lett. **84**, 729 (2004).

8. "Blocking thin film nonuniformities: photovoltaicself-healing", Y. Roussillon, D. Giolando, Diana Shvydka, A. D. Compaan, and V. G. Karpov, Appl. Phys. Lett. **84**, 616 (2004).

9. "All sputtered 14% CdS/CdTe device with ZnO:Al front contact", Akhlesh Gupta and Alvin. D. Compaan, Proceedings of 3rd World Conference on Photovoltaic Energy Conversion, May 11-18, 2003, Osaka, Japan (to be published).

10. "The mesoscale physics of large-area photovoltaics", V. G. Karpov, Diana Shvydka, Yann Roussillon, and A. D. Compaan, Proceedings of 3d World Conference on Photovoltaic Energy Conversion, May 11-18, 2003, Osaka, Japan (to be published).

11. "Oxygenated CdS window layer for sputtered CdS/CdTe solar cells", Akhlesh Gupta, Karthikeya Allada, Sung Hyun and Alvin. D. Compaan Compound Semiconductor Photovoltaics, edited by Rommel Noufi, William N. Shafarman, David Cahen and Lars Stolt, Mat. Res. Soc. Symp. Proc. 763, B8.9 (2003).

12. "14% CdS/CdTe solar cell with ZnO:Al TCO", Akhlesh Gupta and Alvin D. Compaan ,Compound Semiconductor Photovoltaics, edited by Rommel Noufi, William N. Shafarman, David Cahen and Lars Stolt, Mat. Res. Soc. Symp. Proc. 763, B3.9 (2003).

13. "Cu K-edge XAFS in CdTe before and after treatment with $CdCl_2$", Xiangxin Liu, A. D. Compaan, Nadia Leyarovska, and Jeff Terry, Compound Semiconductor Photovoltaics, edited by Rommel Noufi, William N. Shafarman, David Cahen and Lars Stolt, Mat. Res. Soc. Symp. Proc. 763, B3.5 (2003).

14. "Admittance spectroscopy revisited: Single defect admittance and displacement current", V. G. Karpov, Diana Shvydka, U. Jayamaha and A. D. Compaan, J. Appl. Phys. **94**, 5809 (2003).

15. "Photoluminescence Fatigue and Related Degradation in Thin-Film Photovoltaics", Diana Shvydka, C. Verzella , V. G. Karpov and A. D. Compaan, J. Appl. Phys. **94**, 3901 (2003).

16. "Photoluminescence fatigue in CdTe photovoltaics", Diana Shvydka, C. Verzella and V. G. Karpov, Compound Semiconductor Photovoltaics, edited by Rommel Noufi, William N. Shafarman, David Cahen and Lars Stolt, Mat. Res. Soc. Symp. Proc. 763, B5.7 (2003).

17. "Low Light Divergence In Photovoltaic Parameter Fluctuations", Diana Shvydka, V. G. Karpov and A. D. Compaan, Appl. Phys. Lett. **82**, 2157 (2003).

18. "Nonlocal response in CdTe photovoltaics", Diana Shvydka, A. D. Compaan and V. G. Karpov, J. Appl. Phys. **91**, 9059 (2002).

19. "Effects of nonuniformity in thin-film photovoltaics", V. G. Karpov, A. D. Compaan, and Diana Shvydka, Appl. Phys. Lett. **80**, 4256 (2002).

5.2. Poster or oral presentations published on CDROM and the NREL Web site

1. "Cu K-edge EXAFS Study $CdCl_2$ Treatment Effect on CdTe Film", X. Liu, A.D. Compaan, Jeff Terry, National CdTe R&D Team Meeting; Perrysburg, OH; February 26-27, 2004.

2. "Photoluminescence study On Cl And Cu Implanted CdTe Crystal", X. Liu, A.D. Compaan, National CdTe R&D Team Meeting; Perrysburg, OH; February 26-27, 2004.

3. "Modeling of non-uniformity losses in integrated large-area modules", Diana Shvydka and V. G. Karpov, National CdTe R&D Team Meeting; Perrysburg, OH; February 26-27, 2004.

4. "Thermography Mapping and Modeling", Diana Shvydka, J.P. Rakotoniaina and O. Breitenstein, National CdTe R&D Team Meeting; FSEC, Golden, CO; July 10-11, 2003.

5. "Photoluminescence Mapping", Diana Shvydka, A. D. Compaan and V. G. Karpov, National CdTe R&D Team Meeting; FSEC, Golden, CO; July 10-11, 2003.

6. "Low-light diagnostics" Diana Shvydka, A. D. Compaan and V. G. Karpov, National CdTe R&D Team Meeting; FSEC, Golden, CO; November 28-29, 2002.

5.3. Contributed oral or poster presentations (no published manuscript)

1. "Low Light Diagnostics in Thin-Film Photovoltaics", Diana Shvydka, V.G Karpov, A.D. Compaan, APS March meeting, Austin, TX, March 3-7, presentation A8.002, 2003.

2. "A new class of disordered systems: large-area electronics", V. G. Karpov, A. D. Compaan, and Diana Shvydka, APS March meeting, Austin, TX, March 3-7, presentation B15.014, 2003.

3. "Cu K-edge EXAFS in CdTe before and after treatment with $CdCl_2$", Xiangxin Liu, A. D. Compaan, Nadia Leyarovska, and Jeff Terry, 3rd Conference Thin Film and Nanotechnology for Energy Conversion and Storage, Cleveland, OH, September 18-19, poster A3, 2003.

4. "K-edge EXAFS and XANES studies of Cu in CdS/CdTe solar cells", Xiangxin Liu, Akhlesh Gupta and Alvin D. Compaan, Nadia Leyarovska, Jeff Terry , APS March meeting, Indianapolis, IN, March 18-22 2002.

5. "Nonuniformuties and photovoltaic self healing", Yann Roussillon, D.M. Giolando, Diana Shvydka, A.D. Compaan, and V.G. Karpov, 3rd Conference Thin Film and Nanotechnology for Energy Conversion and Storage, Cleveland, OH, September 18-19, poster C5, 2003.

6. "Modulated PL in CdS/CdTe solar cells", A.C. Vasko, S. Hickman, and A.D. Compaan, 3rd Conference Thin Film and Nanotechnology for Energy Conversion and Storage, Cleveland, OH, September 18-19, poster C6, 2003.

5.4. Annual Subcontract Reports Summary published in U.S. Dept. of Energy Photovoltaic Energy Program Contract Summary, FY 2002, 2003

A.D. Compaan and V.G. Karpov, "The Fabrication and Physics of High Efficiency Cadmium-Telluride Thin-Film Solar Cells."

6. PROJECT PERSONNEL

6.1. Research professors

Akhlesh Gupta (Ph.D. Indian Institute of Technology, Delhi)(50% time, 9/1/01–)
Diana Shvydka (Ph.D., U. of Toledo, 5/2002)(9/02–)

6.2. Postdoctoral Associate

Shanli Wang (Ph.D. Shanghai Inst. Of Technical Physics, 97)(50% time, 6/02–)

6.3. Graduate Students (with Principal Advisor)

(Some students received support from other sources but made significant contributions to this work)

Jennifer Drayton (Compaan)
Ph.D. in progress

Xiangxin Liu (Compaan)
M.S. and Ph.D. in progress

Yann Roussillon (Giolando)
Ph.D. in progress

Todd Osborn (Giolando)
M.S. and Ph.D. in progress

Anthony Vasko (Compaan)
M.S. and Ph.D. in progress

Viral Parikh (Compaan)
M.S. and Ph.D. in progress

6.4. Undergraduate students

Levi Gorrell (Karpov), during Summer 2003

NSF Research Experiences for Undergraduates (REU), Summer 2003:
Samantha Dizor (Karpov), "Photoluminescence Fatigue in CdTe/CdS Solar Cells"

6.5. Technical Assistants

Terry Kahle (3/03–)
Robert Burmeister (4/96–) (25% time)